SANDIA REPORT
SAND2011-6136
Unlimited Release
Printed September 2011

Finite Element Analysis of Multilayer Coextrusion

Rekha Rao, Lisa Mondy, Thomas Baer, Robert Collins, Randy Mrozek, Randy Schunk, Matthew Hopkins, and Joseph Lenhart

Prepared by
Sandia National Laboratories
Albuquerque, New Mexico 87185 and Livermore, California 94550

Sandia National Laboratories is a multi-program laboratory managed and operated by Sandia Corporation, a wholly owned subsidiary of Lockheed Martin Corporation, for the U.S. Department of Energy's National Nuclear Security Administration under contract DE-AC04-94AL85000.

Issued by Sandia National Laboratories, operated for the United States Department of Energy by Sandia Corporation.

Available to DOE and DOE contractors from
U.S. Department of Energy
Office of Scientific and Technical Information
P.O. Box 62
Oak Ridge, TN 37831

Telephone: (865) 576-8401
Facsimile: (865) 576-5728
E-Mail: reports@adonis.osti.gov
Online ordering: http://www.osti.gov/bridge

Available to the public from
U.S. Department of Commerce
National Technical Information Service
5285 Port Royal Rd.
Springfield, VA 22161

Telephone: (800) 553-6847
Facsimile: (703) 605-6900
E-Mail: orders@ntis.fedworld.gov
Online order: http://www.ntis.gov/help/ordermethods.asp?loc=7-4-0#online

SAND2011-6136
Unlimited Release
Printed September 2011

Finite Element Analysis of Multilayer Coextrusion

Rekha Rao[1], Lisa Mondy[2], Robert Collins[3], Thomas Baer[4], Randy Mrozek[5], Randy Schunk[6], Matthew Hopkins[6], Joseph Lenhart[5]

[1]Thermal and Fluid Processes, MS0836
[2]Thermal/Fluid Experimental Science, MS0346
[6]Nanoscale and Reactive Processing, MS0836
Sandia National Laboratories
P.O. Box 5800
Albuquerque, New Mexico 87185

[3]Oak Ridge National Laboratories
Nuclear Science and Technology Division
Process Engineering Research Group

[4]Proctor & Gamble Company
Modeling, Simulation and Analysis Department
Beckett Ridge – CETL- IP 332
8256 Union Centre Blvd.
West Chester, OH 45069

[5]Army Research Laboratory
Weapon and Material Research Directorate
Adelphi, MD 20783-1197

Abstract

Multilayer coextrusion has become a popular commercial process for producing complex polymeric products from soda bottles to reflective coatings. A numerical model of a multilayer coextrusion process is developed based on a finite element discretization and two different free-surface methods, an arbitrary-Lagrangian-Eulerian (ALE) moving mesh implementation and an Eulerian level set method, to understand the moving boundary problem associated with the polymer-polymer interface. The goal of this work is to have a numerical capability suitable for optimizing and troubleshooting the coextrusion process, circumventing flow instabilities such as ribbing and barring, and reducing variability in layer thickness. Though these instabilities can be both viscous and elastic in nature, for this work a generalized Newtonian description of the fluid is used. Models of varying degrees of complexity are investigated including stability analysis and direct three-dimensional finite element free surface approaches. The results of this work show how critical modeling can be to reduce build test cycles, improve material choices, and guide mold design.

ACKNOWLEDGMENTS

Thanks go to Mary White and Joel Lash for their complex meshing work, to Tom Hughes with tip on using CUBIT, to Scott Spangler for his SEM images and coextrusion prowess, to David Noble and Stefan Domino with help on boundary conditions, and to Pat Notz for help with the visualization. Phil Cole and his graduate work were the inspiration for the project. The coextrusion team, some of whom are coauthors on this report, and others such as Mark Stavig, John Schroeder, Duane Schneider, and Lothar Bieg who are not, were great to work with and provided many useful discussions. Thanks also go to Mike Winter and Mark Stavig for the rheological measurements of the filled-polymer systems, the modeling would have been much less relevant without your efforts. We appreciate the insightful comments by reviewers Scott Roberts and Christine Roberts, who helped improve the coherence of the report and make the work much clearer. This work was supported by the Laboratory Directed Research and Development program at Sandia National Laboratories.

CONTENTS

Acknowledgments 4

Contents 5

Figures 6

1 Introduction 9

2 Numerical Method 12
2.1 Equations of Motion 12
2.2 Finite Element Implementation 16
2.3 Linear Stability Analysis 17

3 Results From Linear Stability analysis 19
3.1 Verification Problems 19
3.1.1 Linear Stability Analysis of a Liquid Filament 19
3.1.2 Linear Stability Analysis of a Quiescent Liquid Film 22
3.2 Coextrusion Problems 24
3.2.1 Linear Stability Analysis of a Two-Layer Coextruder 24
3.2.2 Linear Stability Analysis of a Three-layer Coextrusion 27

4 Results from 3D free surface flow 29
4.1 3D Free Surface Flow of Offset Die 29
4.2 3D Free Surface Flow in the Splitter 32
4.3 Results for ALE Modeling of the Splitter 34
4.4 Results for Level Set Modeling of the Splitter and Comparison to ALE Modeling 36
4.5 Results for Level Set Modeling of the Splitter for Different Viscosity Ratios 37

5 Results using Capacitor material properties 39
5.1 Rheology of Capacitor Materials 39
5.2 Results for Level Set Modeling of the Splitter 44
5.3 3D Free Surface Flow in the Drawdown Region 45
5.3.1 Newtonian Rheology: Denser More Viscous Fluid over Less Dense, Less Viscous Fluid 46
5.3.2 Shear-thinning Rheology: Denser More Viscous Fluid over Less Dense, Less Viscous Fluid 47
5.3.3 Shear-thinning Rheology: Denser Less Viscous Fluid over Less Dense, More Viscous Fluid 53
5.3.4 Experimental Results from Coextrusion Manufacturing 56

6 Conclusions and Future Work 58

References 59

7 Distribution 62

FIGURES

Figure 1. Schematic of Multilayer Coextruder (left) and mesh showing feed block design and initial splitter (right). 10
Figure 2: Stability map for eigenvalues. Eigenvalues falling into the upper left quadrant are stable, while those in the upper right quadrant are unstable. 18
Figure 3: Geometry and boundary conditions for verification test problem for liquid filament instability (left) with the mesh for the numerical solution (right). 20
Figure 4: Perturbation streamlines (lines) and pressure contours (colors). Free surface deformations are magnified a factor of 500 for emphasis. Deformations become larger as the wave speed is increased. 21
Figure 5: Schematic of geometry and and boundary conditions (top) and mesh (bottom) for the film on a ceiling verification problem. 22
Figure 6: Perturbation streamlines (lines) and pressure contours (colors) for three wave speeds. Free surface deformations are magnified a factor of 500 for emphasis. 23
Figure 7: Schematic of flow in two layer coextruder with boundary conditions (top) and finite element mesh (bottom). 24
Figure 8: Plot of eigenvalues real and imaginary part 26
Figure 9: Perturbation velocity vectors and pressure contours 26
Figure 10: Base flow in a tri-layer co-extruder (pressure contours and velocity vectors) 27
Figure 11: Flow perturbations in a tri-layer co-extruder (pressure contours and velocity vectors at the stability limit) 27
Figure 12: Details of the flow instability in the tri-layer coextruder 28
Figure 13: Proposed four-layer structure for direct fabrication of a capacitor. The blue material is dielectric and the red material is conductive 29
Figure 14: The undeformed mesh for offset die for a possible three layer design, with the inner fluid (red) encapsulated by two layers of fluid (yellow) is shown in the top figure. The bottom figure shows the mesh and velocity vectors for the flow. This design would allow us to directly manufacture a three-layer capacitor without an additional step of adhering an encapsulated layer at the edge of the device. 30
Figure 15: Meniscus shape for the offset die designed to create a capacitor structure directly. The encapsulating fluid is made transparent to better visualize the die swell of the conductive polymer even for Newtonian rheology 31
Figure 16: a) Free surface shape for a low inlet pressure for the yellow polymer. b) Free surface shape for an intermediate pressure where the yellow fluid is taking a larger volume than at lower pressure. c) Free surface shape for a higher pressure where the yellow material has begun to wet the blue die. 32
Figure 17: Coextruder mesh for initial multiplication creating a four-layered structure by splitting and restacking a two-layered one. Velocity vectors on mesh (left) show acceleration and redirection of fluid through the splitter. The view on the right shows a break out of the two fluids to more clearly see the splitter design. 32
Figure 18: Viscosity of neat polystyrene resin as a function of temperature from 180^{o}C–260^{o}C (left) and as a function of 200nm nickel particle content from 10-40 vol% at 210^{o}C (right). 33
Figure 19: Simulation results for a flow splitter mold containing a red and a blue fluid. The properties are identical for both fluids: The viscosity is 10,000 Poise and the density

is 1 g/cc. Because of the design of the splitter, the layers at the out flow are not uniform in thickness even for the same material properties in both fluids. The interfacial tension between layers is assumed to be 45 dyne/cm. 34
Figure 20: Simulation results for parameter continuation of the red phase viscosity from its initial value of 10,000 Poise to 64,000 Poise, where the mesh becomes too distorted to support further simulations. The blue phase is held constant at 10,000 Poise and the density of both phases is 1 g/cc..... 35
Figure 21: Simulation results for parameter continuation of the red phase inflow pressure from its initial value of 10,000 dyne/cm^2 to 17,650 dyne/cm^2, where the mesh becomes too distorted to support further simulations. The red and blue phase properties are held constant at 10,000 Poise and 1 g/cc. The interfacial tension between layers is assumed to be 45 dyne/cm. 36
Figure 22: Comparison of ALE result (left) to level set result (right) for the same properties and inflow pressure (10,000 dyne/cm^2). The red and blue phase properties are equal at 10,000 Poise and 1 g/cc. The interfacial tension between layers is assumed to be 45 dyne/cm. 36
Figure 23: Comparison of black and white experiment SEM (left) to ALE result (middle) to level set result (right) for the same properties and inflow pressure (10,000 dyne/cm^2). The red and blue phase properties are equal at 10,000 Poise and 1 g/cc. The interfacial tension between layers is assumed to be 45 dyne/cm. 37
Figure 24: Comparison of level set results for the same properties and inflow pressure (100,000 dyne/cm^2) (right) with level set results for red phase viscosity of 100,000 Poise with blue phase viscosity at 10,000 Poise (left). Both densities are held constant at 1 g/cc. The interfacial tension between layers is assumed to be 45 dyne/cm..... 38
Figure 25: SEM showing microstructure of well-mixed Ni-Eu-PS composite. 39
Figure 26: SEM of Barium Titanate at 1000x 39
Figure 27: Parallel plate and capillary rheology for neat polystyrene (PS), BT-PS filled polymer, and Ni-Eu-PS filled polymer at 225^{o}C..... 40
Figure 28: Low shear-rate parallel plate rheometry (blue) and high shear-rate capillary rheometry (red) data for 12vol% Ni, 28vol% Eutectic, and 60vol% polystyrene conductive polymer at 225^{o}C. The rheology was fit to a Carreau model that spans both set of data (purple)..... 41
Figure 29: Low shear-rate parallel plate rheometry (pink) and high shear-rate capillary rheometry (turquoise) data for 20vol% $BaTiO_2$ and 80vol% polystyrene conductive polymer at 225^{o}C. The rheology was fit to a Carreau model that spans both set of data (blue)... 42
Figure 30: Relative viscosity versus volume fraction for a suspension of particles and an emulsion of droplets..... 43
Figure 31: Rheology compared to theory for suspensions and emulsions..... 44
Figure 32: Level set simulations for the estimated properties for the conductive red phase (25,0000 Poise, 4.09g/cc) and dielectric blue material (15,0000 Poise, 2.06g/cc). The inflow velocity is 5 cm/s. The picture on the left shows the simulation at an early time when the bottom red sheet breaks. The picture on the right shows it reforming at later times, which ends up being the steady profile. 45
Figure 33: Mesh for draw down region that takes the coextruded material from a square cross-section down to a tape. The flow goes from right to left with the initial cross-section

being 1.27cm by 1.27cm drawdown to 5.08cm by 0.2cm in 2.54cm. The second drawdown is more gradual over 3.81cm to 5.08cm by 0.1cm. 46
Figure 34: Initial condition for coextrusion simulations of draw down region. 46
Figure 35: Bottom fluid free surface profile for Newtonian properties (40,000 Poise, 2.06g/cc) as a function of time at 0.5s, 1.0s, 2.0s, 5s, 7s, 10s: The top fluid has 10 time the viscosity of the bottom fluid and twice the density (400,000 Poise, 4.09g/cc). A barring instability is seen toward the exit of the die and pooling of the light, less dense fluid is seen as the fluid goes into the first draw down section. By 10s the fluid has reached an equilibrium profile exhibiting barring at the edges of the flow and a smooth meniscus in the center of the die. 47
Figure 36: Lower fluid meniscus and evolving viscosity with time at 0.5s, 1.0s, 2.0s, (top row from left to right) 5s, 7s, 10s (bottom row, from left to right). A ribbing instability is seen at 7.0s, but starts to damp out at later times. The simulations never reach steady state, but oscillate between two states with the shear surface jumping forward and backwards near the outflow). 49
Figure 37: Upper fluid meniscus and evolving viscosity with time at 0.5s, 1.0s, 2.0s, 5s, 7s, and 10s. A ribbing instability is seen at 7.0s, but starts to damp out at later times. The simulations never reach steady state, but oscillate between two states with the shear surface jumping forward and backwards near the outflow. 50
Figure 38: Axial slices of the viscosity as it moves down the mold from the entrance to the drawdown region at 27.9s. (Inflow is at the top of the image and we move axially down the extruder.) The viscosity of the top fluid is higher than the bottom fluid based on the rheology of the real materials. 51
Figure 39: Outflow profile as a function of time for 0.5s, 1.0s, 2.0s, 5s, 7s, 10s. 52
Figure 40: Outflow profile at long times (t=29.7s). 52
Figure 41: Lower fluid meniscus and evolving dimensionless viscosity with time at 0.5s, 1.0s, 2.0s, 5s, 7s, 10s. A ribbing instability is seen beginning at 5.0s and develops more fully at 7.0s, but starts to damp out at later times. The simulations never reach steady state, but oscillate between two states with the shear surface jumping forward and backwards near the outflow. 53
Figure 42: Upper fluid meniscus and evolving viscosity with time at 0.5s, 1.0s, 2.0s, 5s, 7s, 10s. A ribbing instability is seen at 5.0s, increases at 7.0s, but starts to damp out at later times. The simulations never reach steady state, but oscillate between two states with the shear surface jumping forward and backwards near the outflow..... 54
Figure 43: Axial slices of the viscosity as it moves down the mold from the entrance to the drawdown region at 27.9s. (Inflow is at the top of the image and we move axially down the extruder.) The viscosity of the bottom fluid is higher than the top fluid. The density of the top fluid is higher than the bottom fluid..... 54
Figure 44: Outflow profile as a function of time for 0.5s, 1.0s, 2.0s, 5s, 7s, 10s 55
Figure 45: Outflow profile at long times (t=29.4s). 55
Figure 46: Coextruded eight-layer capacitor showing instabilities present for fluid with both mismatched viscosities and densities..... 56
Figure 47: SEM of coextruded capacitor for slower flow rate of more viscous fluid. This process reduces the layer instability seen in figure 46..... 57

1 INTRODUCTION

Multi-layered coextrusion combines multiple polymers into a layered structure to produce composite properties that are not found in a single polymer. This method has been implemented successfully by companies like 3M and Dow to produce multilayered structures of ~ 20 μm and 110 nm, respectively [3M 2005; Dow 2007]. We are investigating multilayer coextrusion as a means of producing many-layered, particle-filled polymer structures for use as an energy storage devices or sensors. We focus on producing a capacitor, which is made by having alternate layers of conductive and dielectric material in a stack of 8 to 64 layers. The conductive layers are produced by dispersing conductive particles in a polymer backbone, creating a composite material that has a higher conductivity than the neat polymer. The dielectric material is formed in a similar manner using ceramic particles in a polymer backbone. Because the polymers are filled with metal or ceramic particles, the materials can be highly viscous and have widely varying densities and viscosities between layers. The rheology of filled-polymers can be especially complex since viscosity can vary locally with shear-rate, temperature and volume fractions of particulates. Particles can agglomerate and form percolated networks that further confound an easy description of the flow behavior. The particles can be heavier than the polymer, resulting in a higher density of the composite mixture. In addition, the polymer matrix can be shear-thinning, viscoelastic and also exhibit normal stresses. All these factors taken together make it extremely difficult to match properties between layers, which can lead to flow instabilities such as ribbing, barring, and encapsulation that can lead to variable layer thickness and a poor quality extrudate [Dooley and Rudolf, 2003; Rincon et al., 1998]. Because we are trying to make a capacitor, it is important to have a clean lamellar structure for its electrical performance.

The goal of this work is to develop numerical capabilities suitable for optimizing and troubleshooting the coextrusion process and circumventing flow and material property induced instabilities. For this study, elastic instabilities are ignored and we focus on Newtonian and shear-thinning fluids only. The numerical model of a multilayer coextrusion process was developed based on a finite element discretization and two different free surface algorithms: an arbitrary-Lagrangian-Eulerian (ALE) moving mesh implementation [Sackinger et al, 1996; Cairncross et al, 2000] and an Eulerian level set method [Sethian, 1999]. The free surface algorithms help us to understand the moving boundary problem associated with the polymer-polymer interface.

The equipment we are using is based on that at the University of Minnesota [Zhao and Macosko, 2002]. A schematic of the coextruder and a mesh of the polymer in the feed block and initial splitter are given in Figure 1.

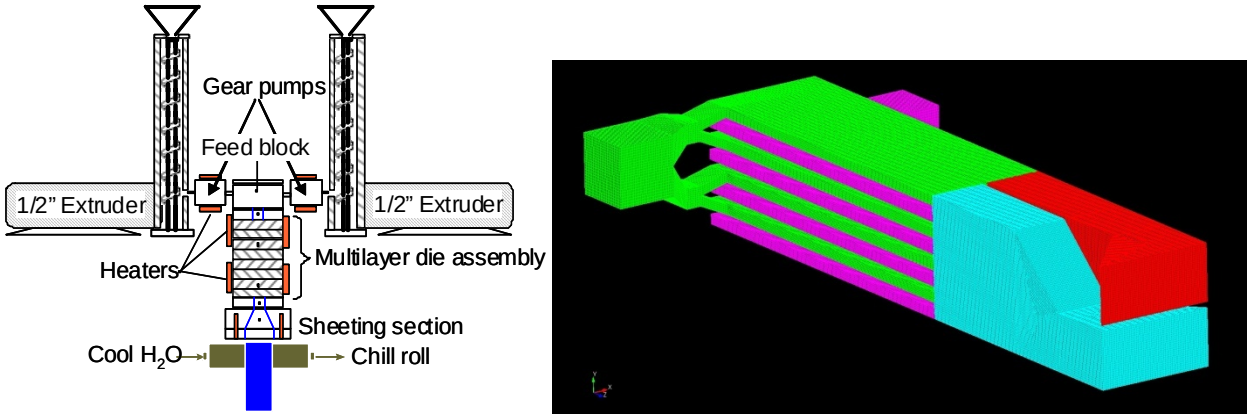

Figure 1. Schematic of Multilayer Coextruder (left) and mesh showing feed block design and initial splitter (right).

The width of the coextruder mold is on the order of 1 cm. The feedstock of conductive and dielectric polymers come in as pellets that are melted in hoppers and then driven into the feed block, with four layers of each polymer creating an eight layer structure initially. The flow comes in perpendicular to the flow direction and must turn quickly. For this reason, separator plates keep the material from mixing until the flow has become more unidirectional and oriented in the axial direction. Once the flow has developed, the polymers enter an open die where the fluid-fluid interface is formed. From there, the material can go through as many as three splitters where the layers are cut vertically and restacked, to double the number of layers. Quieting zones are necessary after the splitters to damp out instabilities and improve the uniformity of the layers. Band heaters and thermocouples are placed throughout the die assembly to ensure the material maintains a constant temperature. In the sheeting section, the initially square cross-section of the die is drawn down to a thin sheet of the same cross-sectional area. The sheet is then extruded onto a chilled roller to thin it even further and quench the flow. The chilled rollers are thought to eliminate many of the instabilities associated with the extrusion flow, since they quench the fluid to a solid state, locking in the polymer-polymer interface shape coming out of the die.

Numerical models of varying degrees of complexity are investigated including stability analysis and direct finite element free surface approaches. Linear stability analysis is used in simplified two-dimensional geometries to help understand the limit on density mismatch between layers. We include a section on verification of our linear stability analysis capability on problems with analytical solutions.

Full three-dimensional finite element free surface flows are used in three different geometries to understand stable operating conditions such as pressure or flow rate mismatch or viscosity mismatch and to examine a novel die design that allows for offsets between layers. The three geometries we examine are:

1) Flow in an offset die, designed to have one polymer encapsulate another.
2) Flow through the splitter where the number of layers is doubled by vertically slicing the flow and then restacking it.
3) Flow in a converging die, where an initially square cross-section is drawn down to a tape with the same area, but having a thinner, wider cross-section.

In the following sections, we review the equations of motion and numerical method, discuss problem set up, and then present results for models of coextrusion processes. We conclude by summarizing our findings and making suggestions for future work.

2 NUMERICAL METHOD

2.1 Equations of Motion

The equations of motion for the flow of incompressible, viscous Newtonian and non-Newtonian fluids are as follows. We have conservation of momentum,

$$\rho \frac{D^* \mathbf{u}^*}{D^* t^*} = \nabla^* \bullet (\eta(\nabla^* \mathbf{u}^* + \nabla^* \mathbf{u}^{*t}) - \nabla^* p^* + \rho \mathbf{g} + \mathbf{f} \tag{1}$$

and conservation of mass for incompressible fluids with constant density, ρ, and viscosity, η.

$$\nabla^* \bullet \mathbf{u}^* = 0 \tag{2}$$

Here **u*** is the fluid velocity, **p*** is the pressure, **t*** is time, **g** is the gravitational acceleration, **f** includes all other body force terms, . The * indicates that the variables are dimensional. All physical properties are dimensional as well.

It is useful to solve the problem in dimensionless form, since the viscosity of the polymer is extremely large and could create difficulties for solving the discretized equations. Because we have two polymer phases, which can have different material properties, we must write equations for each phase. Here we denote one phase as the “light” phase and one phase as the “heavy” phase.

We first write the dimensional equations for both the light phase, where the subscript “l” denotes the light phase density and viscosity,

$$\begin{aligned} &\rho_l \frac{D^* \mathbf{u}^*}{D^* t^*} = \nabla^* \bullet (\eta_l(\nabla^* \mathbf{u}^* + \nabla^* \mathbf{u}^{*t}) - \nabla^* p^* + \rho_l \mathbf{g} + \mathbf{f} \\ &\nabla^* \bullet \mathbf{u}^* = 0 \end{aligned} \tag{3}$$

and heavy phases, where the subscript “h” denotes the heavy phase density and viscosity:

$$\begin{aligned} &\rho_h \frac{D^* \mathbf{u}^*}{D^* t^*} = \nabla^* \bullet (\eta_h(\nabla^* \mathbf{u}^* + \nabla^* \mathbf{u}^{*t}) - \nabla^* p^* + \rho_h \mathbf{g} + \mathbf{f} \\ &\nabla^* \bullet \mathbf{u}^* = 0 \end{aligned} . \tag{4}$$

We perform the nondimensionalization assuming a viscous stress scale based on the light phase viscosity, η_l v/d, v is a characteristic velocity, and d is a charancteristic dimension [Bird et al, 1980]. We assume that gravity is the only body force. The nondimensionalization proceeds creating dimensionless variables u, p, and t from the dimensional variables u*, p*, and t*.

The nondimensionalization introduces new dimensionless numbers into the equations such as the Reynolds' number, the Froude number, the viscosity ratio and the density ratio.

$$\begin{aligned} \mathrm{Re} &= \frac{\rho_l v d}{\eta_l} \\ Fr &= \frac{v^2}{gd} \\ Ca &= \frac{\eta_l v}{\sigma} \\ \beta &= \frac{\eta_h}{\eta_l} \\ \Gamma &= \frac{\rho_h}{\rho_l} \end{aligned} \tag{5}$$

The dimensionless equations of motion for the light fluid are

$$\begin{aligned} &\mathrm{Re}\frac{D\mathbf{u}}{Dt} = \nabla \bullet (\nabla \mathbf{u} + \nabla \mathbf{u}^t) - \nabla p + \frac{\mathrm{Re}}{Fr}\mathbf{e}_g, \\ &\nabla \bullet u = 0 \end{aligned} \tag{6}$$

while the dimensionless equations for the heavy fluid are

$$\begin{aligned} &\Gamma\mathrm{Re}\frac{D\mathbf{u}}{Dt} = \nabla \bullet (\beta(\nabla \mathbf{u} + \nabla \mathbf{u}^t)) - \nabla p + \frac{\Gamma\mathrm{Re}}{Fr}\mathbf{e}_g \\ &\nabla \bullet u = 0 \end{aligned} \tag{7}$$

For Arbitrary Lagrangian-Eulerian (ALE) methods, the material surface is identified with the kinematic condition, a boundary condition that is described in mathematical form as:

$$n \bullet (v - \dot{x}) = 0\,. \tag{8}$$

If surface tension is present at the polymer-polymer interface, we must also specify a capillarity boundary condition.

$$-\mathbf{n} \bullet (\boldsymbol{\tau}_h - \boldsymbol{\tau}_l) = \frac{2H\mathbf{n}}{Ca}\,. \tag{9}$$

This boundary conditions assumes that there are no surface tension gradients.

For this study, this viscosity is either constant, as in a Newtonian fluid, or the viscosity is shear-thinning, represented by a generalized-Newtonian model. Here we use a Carreau-Yasuda model as it is numerically well-behaved over the a large range of shear-rates [Bird et al, 1987].

$$\eta = \eta_\infty + (\eta_0 - \eta_\infty)(1 + (\lambda\dot{\gamma})^a)^{\frac{(n-1)}{a}} \tag{10}$$

The Carreau-Yasuda model has five parameters associated with it: A zero shear-rate viscosity, η_0, an infinite shear-rate viscosity, η_{inf}, a time constant, λ, a power law exponent, n, and another fitting exponent, a. (Note, a Carreau model has a fixed at 2.)

For the non-Newtonian version of the nondimensionalization, we use the zero shear-rate viscosity of the lighter fluid and follow a similar procedure to the Newtonian version resulting in the dimensionless groups and equations below. Note that the Carreau-Yasuda model introduces two additional viscosity ratios, β_1 and β_2 associated with the two zero shear-rate and two infinite shear rate viscosities, as well as two dimensionless time constants, We_l and We_h, associated with the transition from zero shear-rate to high shear rate behavior for the light and heavy fluid respectively.

$$\begin{aligned}
\mathrm{Re} &= \frac{\rho_l v d}{\eta_{0l}} \\
Fr &= \frac{v^2}{gd} \\
Ca &= \frac{\eta_{0l} v}{\sigma} \\
\beta &= \frac{\eta_{0h}}{\eta_{0l}} \\
\Gamma &= \frac{\rho_h}{\rho_l} \\
We_h &= \frac{\lambda_h v}{d} \\
We_l &= \frac{\lambda_l v}{d}
\end{aligned} \tag{11}$$

The nondimensionalization for the light fluid is

$$\mathrm{Re}\frac{D\mathbf{u}}{Dt} = \nabla \bullet (\beta''(\nabla\mathbf{u} + \nabla\mathbf{u}^t)) - \nabla p + \frac{\mathrm{Re}}{Fr}\mathbf{e}_g$$
$$\beta'' = \beta_2 + (1-\beta_2)(1+(We_l\dot{\gamma})^a)^{\frac{(n-1)}{a}} \quad , \qquad (12)$$
$$\beta_2 = \frac{\eta_{\infty h}}{\eta_{0l}}$$
$$\nabla \bullet u = 0$$

While the dimensionless equations of motion for the heavy fluid are

$$\Gamma\mathrm{Re}\frac{D\mathbf{u}}{Dt} = \nabla \bullet (\beta'(\nabla\mathbf{u} + \nabla\mathbf{u}^t)) - \nabla p + \frac{\Gamma\,\mathrm{Re}}{Fr}\mathbf{e}_g$$
$$\beta' = \beta_1 + (\beta-\beta_1)(1+(We_h\dot{\gamma})^a)^{\frac{(n-1)}{a}} \qquad (13)$$
$$\beta_1 = \frac{\eta_{\infty h}}{\eta_{0l}}$$
$$\nabla \bullet u = 0 \quad .$$

The free surfaces associated with polymer-polymer or polymer-air interfaces are handled with a pseudo-solid mesh motion algorithm, which moves the mesh according to the material interfaces at these boundaries and elsewhere moves as a nonlinear elastic solid. The mesh equations for a neo-Hookean constitutive equation are:

$$\nabla \bullet \mathbf{S} = 0$$
$$\mathbf{S} = \lambda e\mathbf{I} + 2\mu\mathbf{E} \qquad (14)$$
$$\mathbf{E} = \frac{1}{2}[\nabla\mathbf{d} + \nabla\mathbf{d}^t - \nabla\mathbf{d}\bullet\nabla\mathbf{d}]$$

For details of our mesh motion algorithm and implementation please see Cairncross *et al.,* 2000 and Baer *et al.,* 2000 [5,6].

For problems with large deformations or when we need to model coalescence of layers, it is preferable to use an Eulerian method or front capturing scheme since these methods handle topological changes without the need for remeshing and remapping. For these problems, we use the level set method of Sethian [1999], a front capturing scheme, which is used to determine the evolution of the interface with time. The level set is a scalar distance function, the zero of which coincides with the free surface or fluid-gas interface, *e.g.*

$$\phi(x,y,z) = 0\,. \qquad (15)$$

We initialize this function to have a zero value at the fluid-fluid interface, with negative distances residing in the heavy phase and positive distances in the light phase. An advection equation is then used to determine the location of the interface over time.

$$\frac{d\phi}{dt} + v \bullet \nabla \phi = 0 \tag{16}$$

Derivatives of the level set function can give us surface normals, n, and curvature, H, at the interface useful for applying boundary conditions.

$$\begin{aligned} n &= \nabla \phi \\ H &= \nabla \bullet \nabla \phi \end{aligned} \tag{17}$$

Material properties vary across the phase interface from the properties of the fluid to the properties of the displaced gas. This variation is handled using a smooth Heaviside function that modulates material properties to account for the change in phase.

$$\rho(\phi) = \rho_{fluid} + (\rho_{gas} - \rho_{fluid}) H_\alpha(\phi), \qquad -\alpha < \phi < \alpha \tag{18}$$

$$\mu(\phi) = \mu_{fluid} + (\mu_{gas} - \mu_{fluid}) H_\alpha(\phi), \qquad -\alpha < \phi < \alpha \tag{19}$$

$$H_\alpha(\phi) = \frac{1}{2}\left(1 + \frac{\phi}{\alpha} + \frac{1}{\pi}\sin\left(\frac{\pi\phi}{\alpha}\right)\right) \tag{20}$$

This is a diffuse interface implementation of the level set method, which allows for a mushy interfacial zone of length 2α, in which the properties will vary from fluid to gas values. Here we choose α to be 2-3 elements wide. Note that this method can be applied to both Newtonian and non-Newtonian fluids.

We have also implemented another level set method where equation averaging is done using a Heaviside. The momentum equation, including property modulation becomes,

$$\begin{aligned} &(H_A\rho_A + H_B\rho_B)\left(\frac{\partial u}{\partial t} + u \bullet \nabla u\right) = H_A \nabla \bullet \underline{\underline{\pi}}_A + H_B \nabla \bullet \underline{\underline{\pi}}_B + (H_A\rho_A + H_B\rho_B)\underline{g} \\ &\underline{\underline{\pi}}_i = \eta_i(\nabla u + \nabla u^t) - p\underline{\underline{I}} \quad \textit{where } i=A,B \\ &\nabla \bullet u = 0 \end{aligned} \quad . \tag{1}$$

2.2 Finite Element Implementation

The equations of motion and the mesh equations are solved with the finite element method, using GOMA and ARIA, a suite of computer codes designed to solve free and moving boundary problems [Schunk et al, 2006; Notz et al, 2007]. The equations are solved in a fully-coupled, Newton-Raphson manner, except for the level set equations, which is sometimes segregated. The Navier-Stokes equations were stabilized with the Dohrmann-Bochev pressure stabilized pressure-projection [Dohrmann and Bochev, 2004] or the pressure-stabilized Petrov-Galerkin

method (PSPG) [Hughes, 2000] to allow for equal order, bilinear, interpolation of all variables; velocity, pressure and mesh. As these are large, 3D problems, direct solution methods for matrix inversion are precluded. Instead, we use Krylov-based iterative solver and preconditioning. For this work, we use an ILUT preconditioner with up to three levels of fill and a GMRES solve. The moving mesh problems are solved in a steady manner, ignoring time derivative, as a stable coextrusion process must run at steady-state. Damping of 0.05 is necessary in order to achieve a convergent solution. The problem must be either rescaled or nondimensionalized in order to get good convergence of the iterative solvers. The level set method is inherently transient, so when we use this method we must solve temporal equations.

2.3 Linear Stability Analysis

We have developed a generalized linear stability analysis capability in the finite element code GOMA [Gates et al, 2001]. Steady-state analysis can lead to solutions that do not exist physically. Transient analysis, on the other hand, can be time consuming since multiple time steps must be taken in order to achieve an equilibrium solution. Linear stability analysis of a steady state solution can give you information similar to transient analysis, but at a lesser cost. By solving an eigenvalue problem based on the steady solution, we can determine when solutions are stable and when they are not.

To apply this method, we first decompose the solution into a bulk solution and a perturbation as shown below for the velocity vector, the pressure and the displacement vector:

$$\begin{aligned} \mathbf{v} &= \mathbf{v}_{\mathbf{bulk}} + \boldsymbol{\varepsilon}_{\mathbf{v}} \\ p &= p_{bulk} + \varepsilon_p \\ \mathbf{d} &= \mathbf{d}_{\mathbf{bulk}} + \boldsymbol{\varepsilon}_{\mathbf{d}} \end{aligned} \quad . \tag{21}$$

We then substitute these variables into equations of motion and the mesh equations (equations 1, 2, 14), subtract off the bulk equation terms, and linearize the resulting equations by neglecting any higher-order terms in the small perturbation. These operations lead to the following, generalized eigenvalue problem:

$$\begin{aligned} &J\,\vec{x} = \lambda M\,\vec{x}, \text{ where } \quad J_{i,j} = \left(\frac{\partial R_i}{\partial x_j}\right) \\ &M = \text{ "Mass" matrix, } M_{i,j} = \left(\frac{\partial R_i}{\partial \dot{x}_j}\right) \end{aligned} \tag{22}$$

Computing mass matrix entries is non-trivial due to boundary conditions. In addition, the mass matrix is nonsymmetric, has some zero diagonals, and is non-positive definite. This problem is solved with the shift-and-invert or Cayley Arnoldi-based algorithms in ARPACK in Goma (need a citation here). We perform a modal analysis, *viz.* we compute the eigenvalue and eigenvector pairs, (λ_i,$\boldsymbol{x}_i$) from equation 22. The eigenvalues are made up of a real part and an imaginary part.

From these eigenvalues we can tell if the solution will be stable or unstable. If the largest real part of all eigenvalues is > 0, the base solution is unstable; conversely, if all real parts are <= 0, then the base solution is stable. The size of the real part indicates the timescale for growth of instabilities, or damping rates that return a perturbed solution to the base solution. Thus, by determining the maximum real part over all eigenvalues, we can determine if the base solution is stable, and also capture the largest growth rate.

$$\begin{aligned} e^{\lambda t} &= e^{t(\lambda_r + i\lambda_{im})} \\ \lambda_r &> 0 \\ \lambda_{r1} &= \lambda_{\max} > 0 \end{aligned} \tag{23}$$

Figure 2 gives a graphical representation of the stability map for eigenvalue analysis.

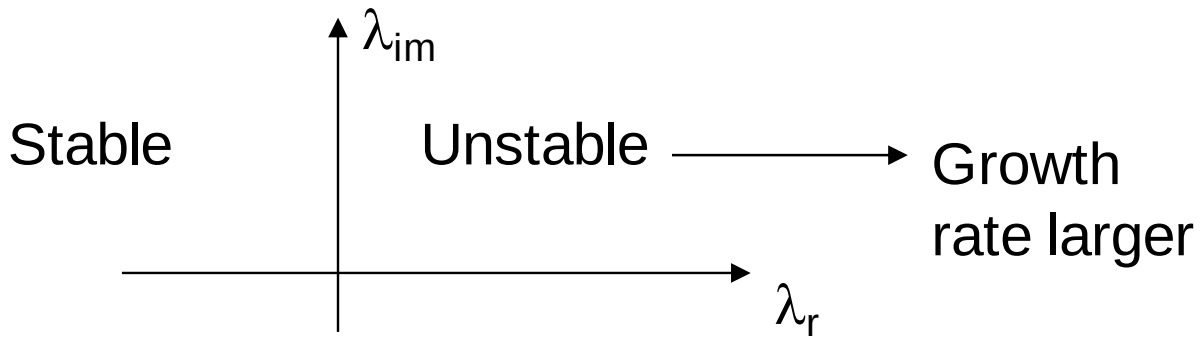

Figure 2: Stability map for eigenvalues. Eigenvalues falling into the upper left quadrant are stable, while those in the upper right quadrant are unstable.

For this study, we often want to determine when a parameterized base solution transitions from stable to unstable. That is, we want to determine when the largest real part of the eigenvalues switches from negative to positive? For all eigenvalue, eigenvector pairs, the eigenvector provides the modal shape, or the physical representation, of the perturbation that grows or damps.

3 RESULTS FROM LINEAR STABILITY ANALYSIS

3.1 Verification Problems

We began our stability analysis by verifying the algorithms in GOMA using problems with analytical solutions. Two classical problems were investigated: Stability of a liquid filament and stability of a liquid film. The results of these analyses are discussed in the next two section.

3.1.1 Linear Stability Analysis of a Liquid Filament

Liquid filaments in air break up into droplets due to a capillary instability (Rayleigh instability). Analytical solutions by normal mode analysis are available for inviscid jets [Rayleigh, 1882] and for Newtonian jets [Chandrasekhar, 1961]. Varicose or axisymmetric modes, for which the dimensionless axial wave number $k < 1$, are unstable. The most unstable mode corresponds to $k_{max} = 0.7$ for inviscid jets. When viscous effects are important, however, longer waves are favored. This well-studied problem is used to verify GOMA's ability to predict free surface instabilities using the methods discussed in the previous section.

In this simulation, the domain is constrained axially with a length of $2\lambda_{max}$, and zero axial velocity at the upper and lower boundaries is imposed (see figure 3). The axisymmetric mesh used for the numerical solution of the general eigenvalue problem in GOMA is also shown in figure 3. For axisymmetric problems we assume radial symmetry, assume no angular dependence of the flow, and solve for only half of the domain in a two-dimensional geometry.

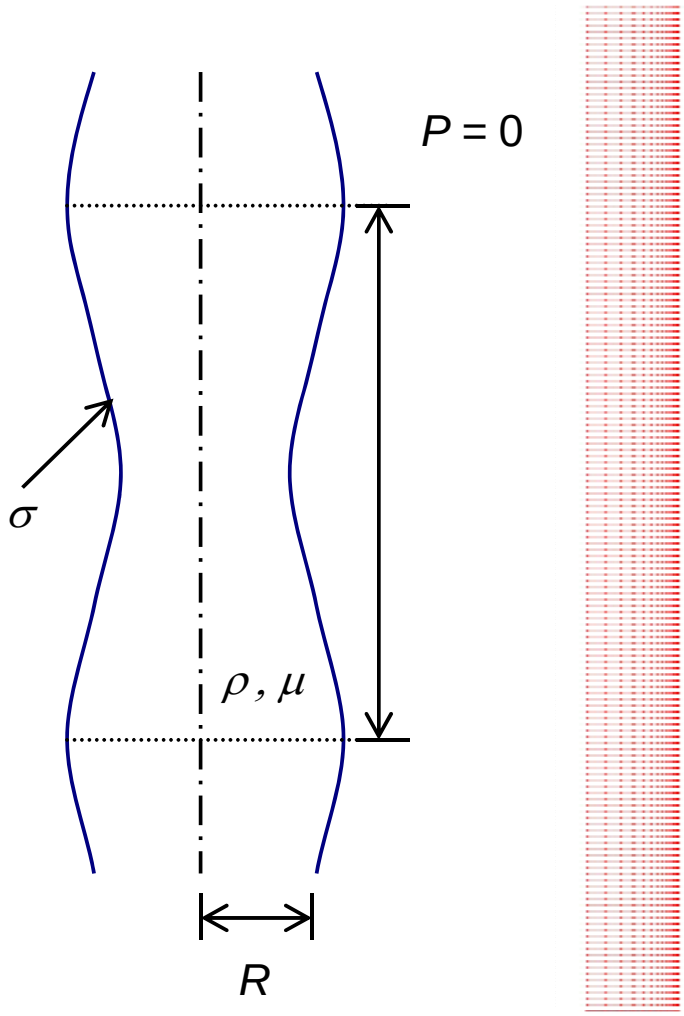

Figure 3: Geometry and boundary conditions for verification test problem for liquid filament instability (left) with the mesh for the numerical solution (right).

Axisymmetric filaments were examined with a radius of 1 mm water jets, a density of 1 g/cm^3, a viscosity of 1 cP, and surface tension of 70 dynes/cm. For this system, the maximum wave speed based on analytical theory is k_{max} = 0.649 [Chandrasekhar, 1961]. Table I shows a comparison between the numerical results from solving a generalized eigenvalue problem in GOMA and the analytical results from Chandrasekhar [1961] for eigenvalues as a function of wave speed.

Table 1. Comparison between numerical (GOMA) and analytical eigenvalues as a function of wave speed.

k	GOMA ω (s^{-1})	Chandrasekar ω (s^{-1})	Percent Error ((analytical – numerical)/analytical)*100%)
k_{max}	89.75	90.12	0.41%
$(3/4)k_{max}$	81.10	81.39	0.36%

$(5/4)k_{max}$	75.82	76.15	0.43%
$(1/2)k_{max}$	59.88	60.26	0.63%
$(1/4)k_{max}$	31.52	31.87	1.10%

From Table I we can see that the numerical eigenvalue problem matches analytical values to 1%. This is excellent agreement given that no mesh refinement studies or tuning parameters were used for the numerical results. Figure 4 shows the eigenvectors associated with three of the wave speeds: $(3/4)k_{max}$, k_{max}, and $(5/4)k_{max}$.

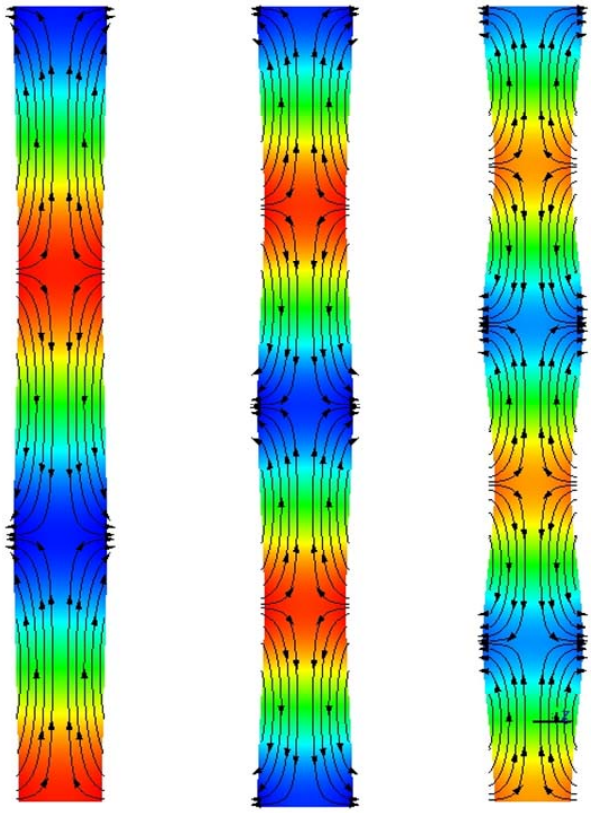

$k = 3/4\ k_{max}$ $k = k_{max}$ $k = 5/4\ k_{max}$

Figure 4: Perturbation streamlines (lines) and pressure contours (colors). Free surface deformations are magnified a factor of 500 for emphasis. Deformations become larger as the wave speed is increased.

Figure 4 shows the perturbation streamlines, pressure contours, and free surface deformations as the wave speed is increased. From this figure, we can see indications of how the filament turns into droplets as the widest portions of the domain are growing while the narrowest portions are decreasing in size.

3.1.2 Linear Stability Analysis of a Quiescent Liquid Film

Perhaps the simplest verification problem is the stability of a quiescent liquid film suspended from a horizontal surface in an unfavorable position gravitationally. Air surrounds the liquid film. Analytical solutions by normal mode analysis are available from Chandrasekhar [1961] and others. In the absence of surface tension, which can stabilize the film, all disturbances (gravity waves) are unstable. Surface tension stabilizes short-wave length perturbations, while long wave length perturbations are always unstable.

Figure 5 shows a schematic of the geometry and boundary conditions, as well as the mesh for the GOMA simulations. We solve for the liquid phase only and infer the gas phase indirectly from the boundary condition of zero pressure and the kinematic condition on the free surface.

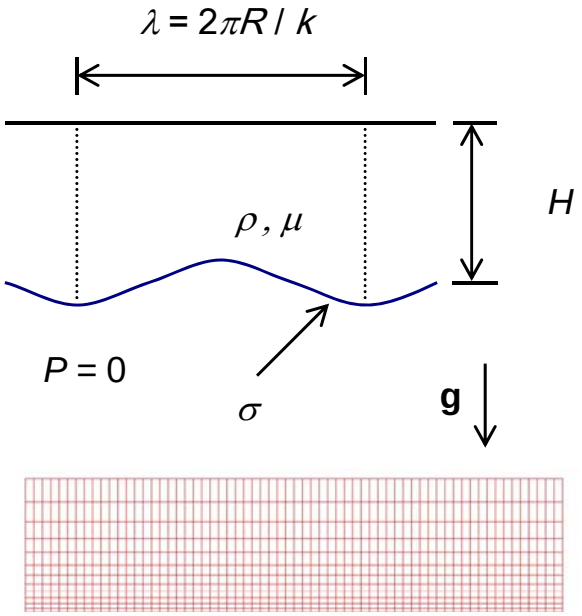

Figure 5: Schematic of geometry and and boundary conditions (top) and mesh (bottom) for the film on a ceiling verification problem.

The dispersion relation for the kth growth rate for negligible viscosity fluids is given below as a function of the material properties, gravity, and hyperbolic tangent functions of the height of the film.

$$\omega_k^2 = -\left(k^2\sigma - \rho g\right)\frac{k}{\rho}\left(\frac{\sinh\left(kH\right)}{\cosh\left(kH\right)}\right) \tag{24}$$

This instability is driven by the unfavorable placement of a high density fluid over a low density one and takes the classical Rayleigh-Taylor form.

We have also examined this problem computationally using GOMA and ARPACK [Gates et al., 2001]. Films examined were water (ρ = 1 g/cm^3 , μ = 1 cP , σ = 70 dynes/cm) with a depth equal to the wavelength of the "most dangerous" wavenumber k_{max} and a domain length of four times this wavelength. Figure 6 shows the eigenvectors for several wave numbers.

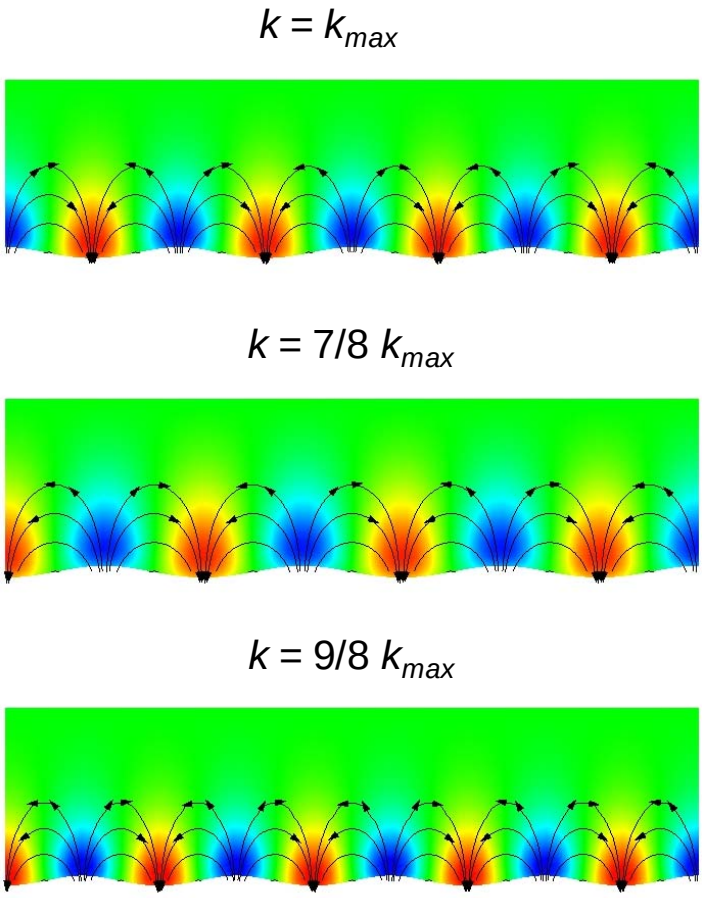

Figure 6: Perturbation streamlines (lines) and pressure contours (colors) for three wave speeds. Free surface deformations are magnified a factor of 500 for emphasis.

The results shown in figure 6 agree with the analytical unstable modes allowed by the domain constraints with a high level of accuracy, as shown in Table 2.

Table 2. Numerical results compared to analytical values of eigenvalues as a function of wave speed for classical Rayleigh-Taylor instability of a film of liquid in air subject to gravity.

k	GOMA ω (s^{-1})	Analytical ω (s^{-1})	Percent Error ((analytical – numerical)/analytical)*100%)
k_{max}	37.51	37.6	0.24%
$(7/8)k_{max}$	37.1	37.17	0.19%

$(9/8)k_{max}$	37.02	37.14	0.32%
$(3/4)k_{max}$	35.89	35.94	0.14%

The difference between the numerical and analytical results is less than 0.4%.

3.2 Coextrusion Problems

Once the method was verified, we used linear stability analysis to investigate simplified coextruder geometries.

3.2.1 Linear Stability Analysis of a Two-Layer Coextruder

The situation is considerably more complicated when shear flow is present, as with the simple two-layer co-extruder shown in figure 7. Here, viscous stresses can act in some instances to stabilize the free surface, and some density stratification is possible without Rayleigh-Taylor instabilities occurring.

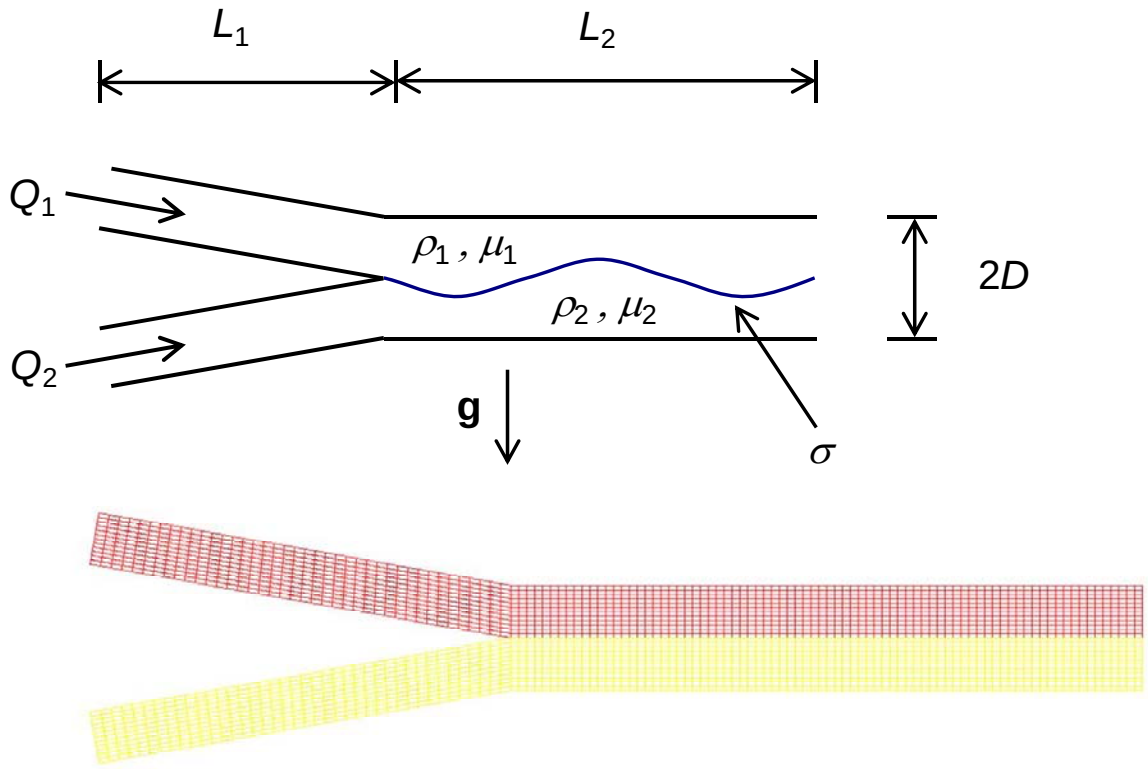

Figure 7: Schematic of flow in two layer coextruder with boundary conditions (top) and finite element mesh (bottom).

Again, we examine the simple co-extruder shown above with GOMA and ARPACK. Here, both the upper (1) and lower (2) fluids are Newtonian and have the same viscosity, with fluid 1 more

dense than fluid 2. The velocities at inflow are constant plug flows and the same for both fluids and there is no slip at the solid boundaries. Zeroth order continuation in the density ratio ρ, ρ_1/ρ_2, is used to find the limit of stability for a heavy fluid flowing over a lighter one. Fluid properties are given below.

$\langle v \rangle_1 = \langle v \rangle_2 = 1$ cm/s

$L_1 = 3$ cm

$L_2 = 2$ cm

$D = 0.25$cm

$\mu_1 = \mu_2 = 10$ P

$\sigma = 30$ dynes/cm

$\rho_2 = 1$ g/cm^3

Figure 8 shows the variation of the leading eigenvalue as a function density. Note that the flow is stable until $\rho \sim 3.82$. It was also seen (though not shown here) that considerably higher density ratios are required as the viscosity is increased, if both fluids have the same viscosity. This is due to viscous effects damping out Rayleigh-Taylor instabilities.

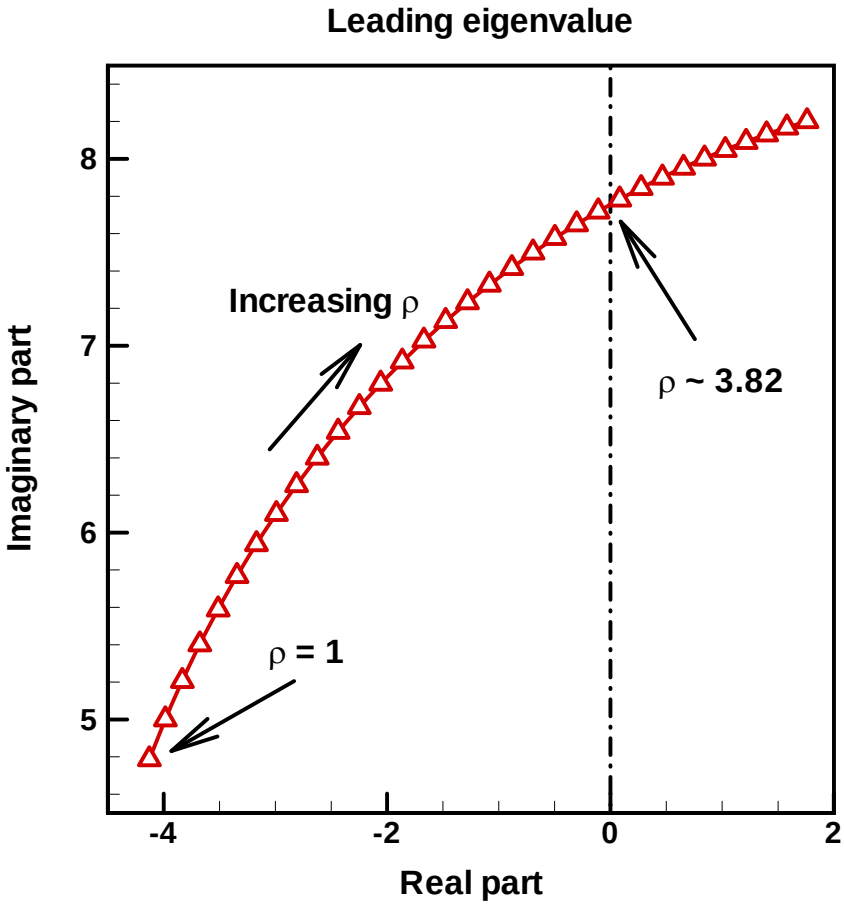

Figure 8: Plot of eigenvalues real and imaginary part

To get an idea of the how the flow becomes unstable, we can examine the eigenvectors for the two-layer coextruder (figure 9). The instability occurs at the interface between the two fluids and seems to begin at the outflow.

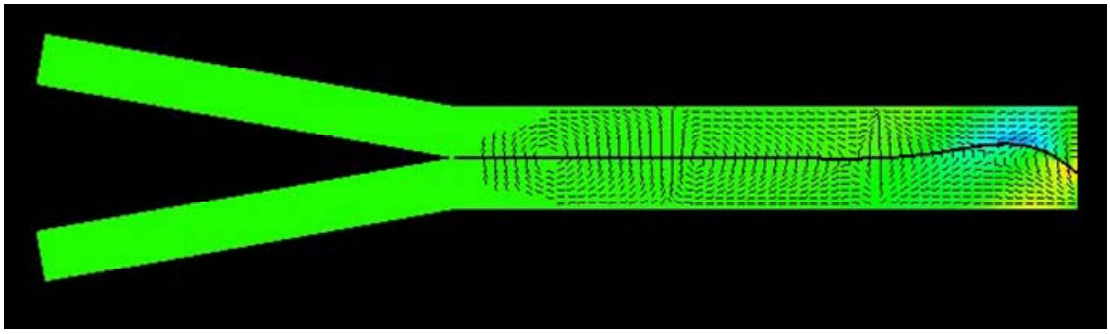

Figure 9: Perturbation velocity vectors and pressure contours

We did try to examine the flow field for unequal values of the viscosity in both phases. For this problem, we had difficulty finding the unstable modes because the out flow boundary condition lead to junk eigenvalues that must be filtered out to find the true “eigenvalues.” This problem has been documented by Musson [2000]. His approach was to manually filter out these junk eigenvalues by adding a location based filter. We have not yet implemented that approach.

3.2.2 Linear Stability Analysis of a Three-layer Coextrusion

Controlling flow instabilities *e.g.* Rayleigh-Taylor or Kelvin-Helmholtz (for flows where the viscosity is mismatched) in multiple-layer co-extrusion processes is critical to proper function and producing lamellar products with uniform layers. Unlike simple two-layer co-extrusion, potentially unstable density stratification is unavoidable in multiple-layer extruders.

Using GOMA with ARPACK, the stability of flows in three-layer co-extruders can be examined with a high degree of accuracy. The base flow for the coextruder is given in figure 10. From this figure, we see that there is some die swell as the fluid exits the region with plates separating the flow and enters the region where the two fluids are in contact.

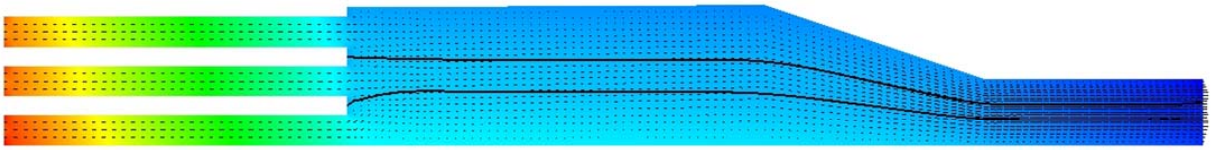

Figure 10: Base flow in a tri-layer co-extruder (pressure contours and velocity vectors)

The stability of the base flow to the density ratio is determined by continuation with LSA. For fluid properties like those used in the two-layer extruder shown above, this 5cm x 21cm extruder becomes unstable when the density difference between the top and bottom layers to center layer reaches 4.33, which is significantly higher than the two layer coextruder that is stable only until 3.92.

We can examine the eigenvectors associated with the leading eigenvalue when the flow begins to go unstable to understand what the instability might look like (see figure 11).

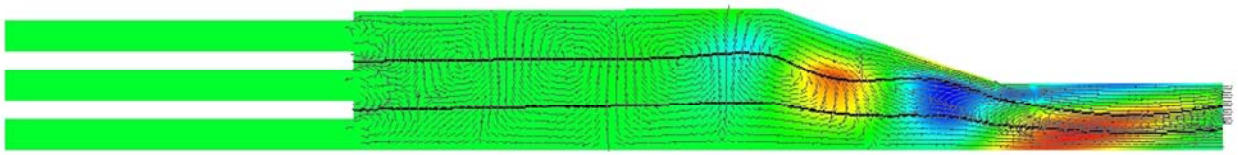

Figure 11: Flow perturbations in a tri-layer co-extruder (pressure contours and velocity vectors at the stability limit)

From this figure, we can see that the instability seems to arise at the top interface in the first drawdown region and then continue in the second drawdown region. The top layer instability also seems to destabilize the bottom interface, which is in a stable configuration with respect to density stratification. These instabilities will lead to problems with the layer structure, such as variable size, of the product. Figure 12 shows the details of the instability.

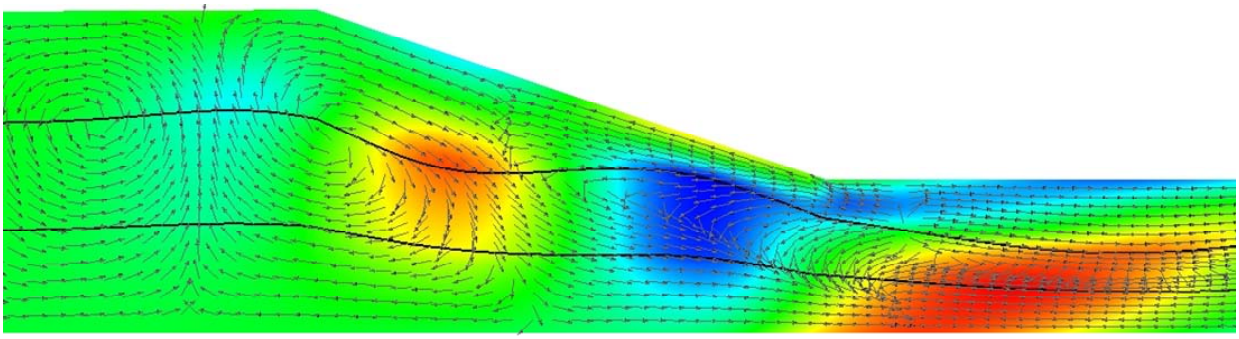

Figure 12: Details of the flow instability in the tri-layer coextruder

Again, because of the issue discussed in the previous section regarding junk eigenmodes, we were unable to examine unequal viscosity ratios for the fluid and are hoping to that in future.

4 RESULTS FROM 3D FREE SURFACE FLOW

4.1 3D Free Surface Flow of Offset Die

For this problem, we investigate the possibility of creating a conductive layer encapsulated within dielectric material. A schematic of this is show in figure 13 for a four-layered structure that is directly fabricated as a capacitor.

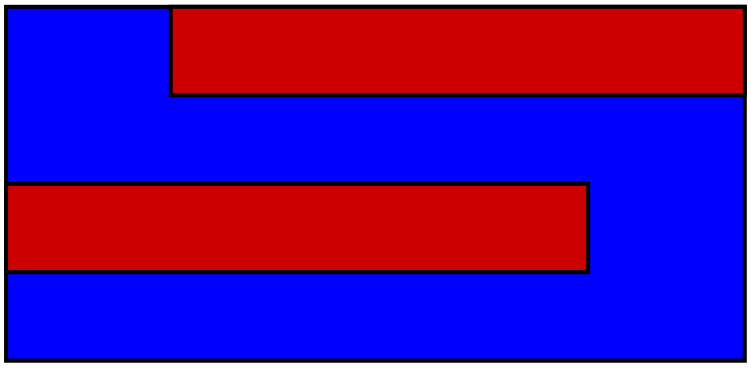

Figure 13: Proposed four-layer structure for direct fabrication of a capacitor. The blue material is dielectric and the red material is conductive.

To simplify the simulation, we look at a three layer structure, since the results should be applicable to materials with higher number of layers. (The one exception to this is the when the flow splitter are applied. The splitters would destroy any encapsulated structure from the inflow.) Alternatively, we can post-process the three-layer structure into larger stacks using an adhesive for the adhering the dielectric layers together.

The initial undeformed mesh, given in figure 14, has 76593 hexahedral elements resulting in 85108 nodes and 368080 degrees of freedom. The blue inlet regions flow into the yellow regions, and are all the same material. The turquoise inlet flows into the red material. Gradual drawdown of the encapsulating fluid layer (shown in turquoise) is carried out to potentially create an offset for the capacitor. The encapsulated fluid changes colors from turquoise to red in the free surface region. The blue encapsulating fluid maintains it cross-section in the die and then the fluid transitions to yellow block in the free surface region. Free surface ALE simulations with a moving mesh will show if encapsulation of the red fluid by the yellow fluid will occur and what the final cross-section will be. The inflow turquoise and navy blue regions solves a different set of equations than the red and yellow regions, where the mesh equations are solved in order to locate the free surface along with the velocity and pressure unknowns. In the inflow region, velocity and pressure are the only unknowns of interest and the mesh is fixed. This was done to decrease the number of unknowns that must be solved.

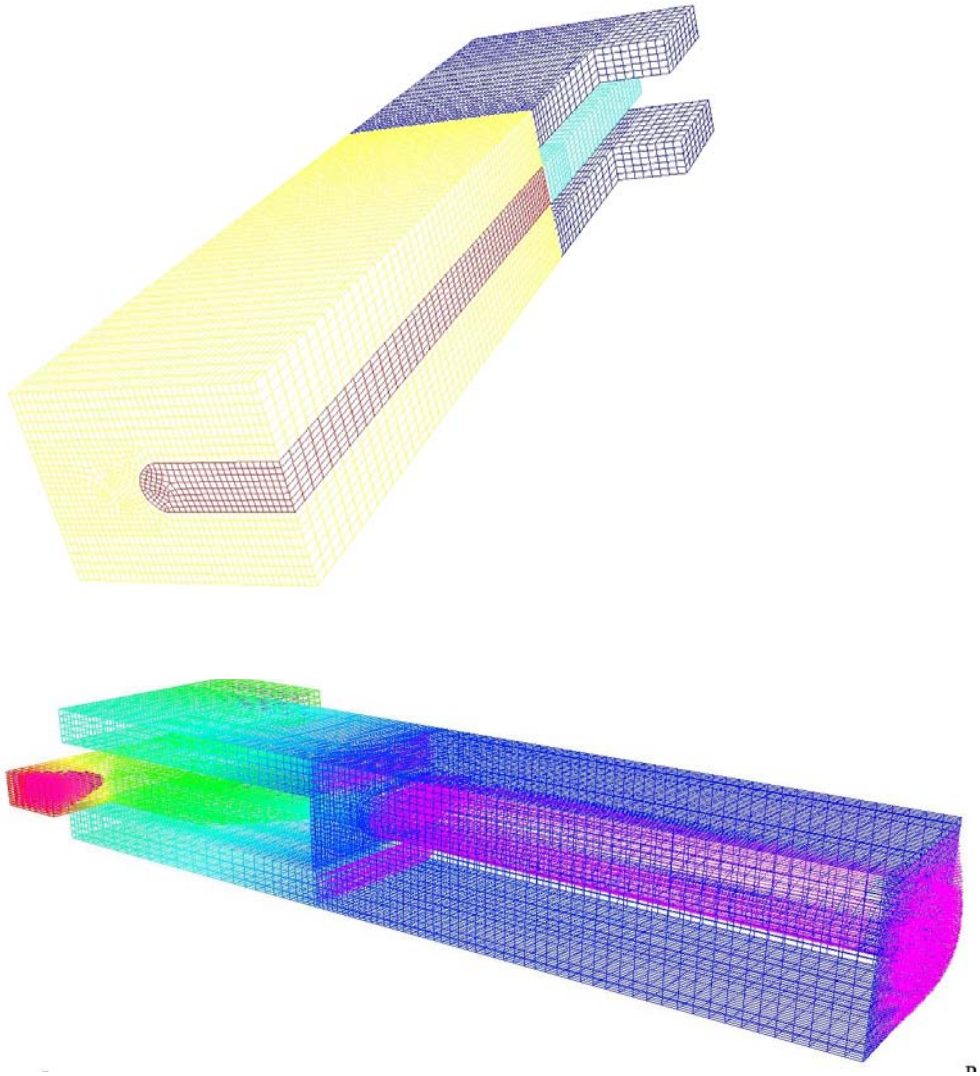

Figure 14: The undeformed mesh for offset die for a possible three layer design, with the inner fluid (red) encapsulated by two layers of fluid (yellow) is shown in the top figure. The bottom figure shows the mesh and velocity vectors for the flow. This design would allow us to directly manufacture a three-layer capacitor without an additional step of adhering an encapsulated layer at the edge of the device.

For this scoping simulation, the viscosities are set arbitrarily to be 100cP in the encapsulating polymer and 200cP for the inner fluid. The densities are assumed to be 1 g/cm^3 for both polymers. The interfacial tension is set to be 45 dyne/cm for the interface between polymers and both fluids are Newtonian. For boundary conditions on the inlet and outlet planes, constant pressure conditions are applied. The inlet pressure on outer fluid is set at both inlet ports to be 2000 dyn/cm^2 while the inlet pressure on the inner fluid entry plane is set to 4000 dyne/cm^2. At the outlet, the pressure is set on both fluid layers to be -440,000 dyne/cm^2. No slip is applied on all solid surfaces and the kinematic condition is applied on interfacial surfaces along with surface tension [Cairncross et al, 2000], though a small amount of slip may be added initially to get the problem started without having to much stress on the fluid-fluid interface that contacts the wall. In the inflow region, the mesh does not move and there are plates separating the two fluids. After

the entry section, the fluids meet in a square mold creating a material interface between the two fluids. The interfacial tension between the fluids is assumed to be 45 dyne/cm.

Results for this problem are given in figure 15. In this figure, we have made the encapsulant transparent in order to better visualize the shape of the meniscus. Here we can see that the inner fluid swells after coming out of the die, even for Newtonian rheology. The inner fluid's cross-section is rounded and looks like a half oval.

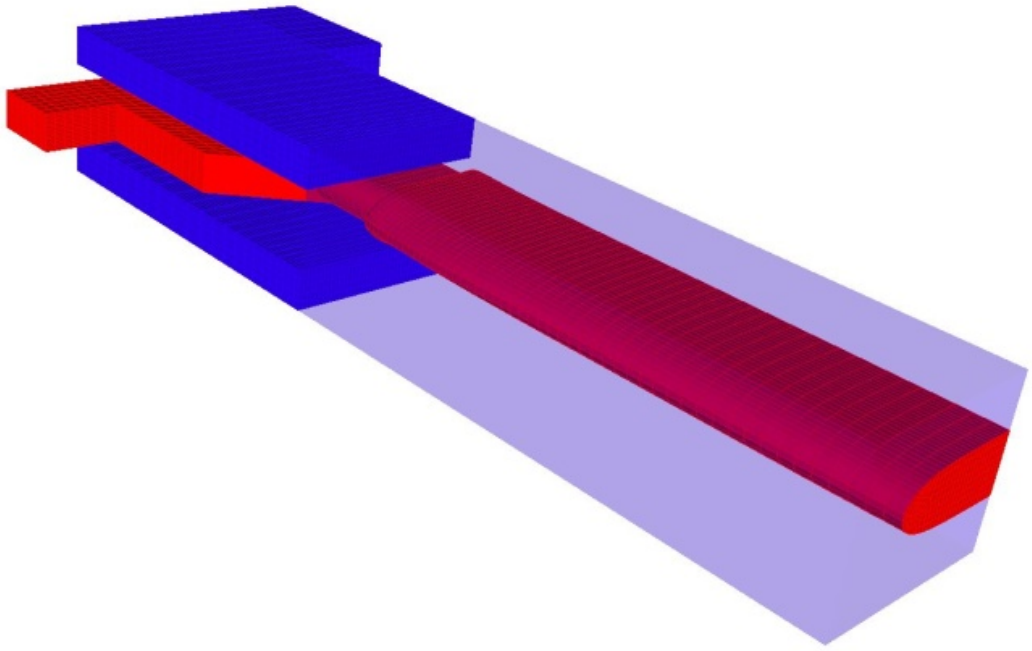

Figure 15: Meniscus shape for the offset die designed to create a capacitor structure directly. The encapsulating fluid is made transparent to better visualize the die swell of the conductive polymer even for Newtonian rheology

Here we look at parameter continuation in the inflow pressure of the top blue material. From figure 15, we see an initially well-behaved free surface at high inlet pressure (16a). However, as we decrease the pressure the yellow material begins to swell (figure 16b) and eventually wet the die lip of the blue material (figure 16c). This can lead to extreme processing difficulties from inhomogeneous layer thickness to actual choking off of the blue fluid. This makes it clear how important it is to carefully meter and balance the flow rates in order to avoid processing issues.

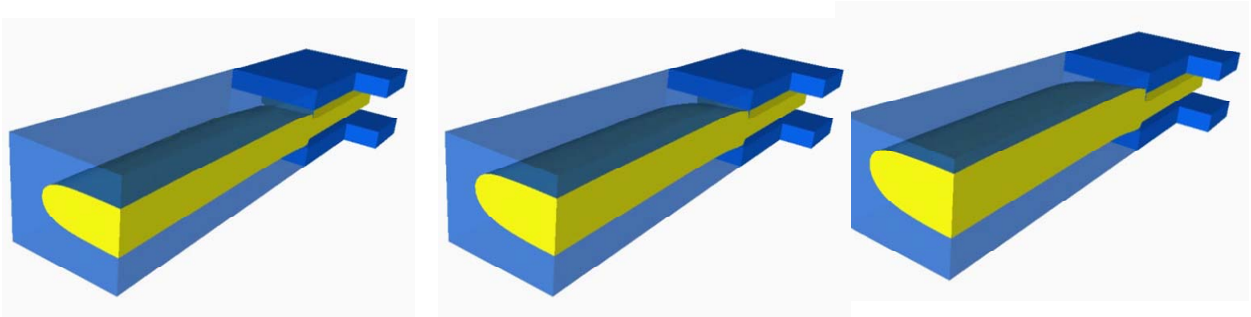

Figure 16: a) Free surface shape for a low inlet pressure for the yellow polymer. b) Free surface shape for an intermediate pressure where the yellow fluid is taking a larger volume than at lower pressure. c) Free surface shape for a higher pressure where the yellow material has begun to wet the blue die.

Because the encapsulant design only works for direct injection from the inflows without any splitters, it can only make eight layer structures. For that reason, we decided not to manufacture an offset die for the coextruder, but instead investigate bonding the encapsulation region on after coextruding a base structure.

4.2 3D Free Surface Flow in the Splitter

3D free surface flows can give us a great deal of information about the shape of the extrudate and how materials properties and processing parameters affect final film thickness and distribution. Here, we have undertaken such a simulation in a simplified geometry similar to our current coextruder, but containing a multiplication region to take the inflow two-layer structure to a four-layered one. It has been observed experimentally that the splitter can induce flow instabilities, so quieting regions are usually added after the flow splitter to damp out the instabilities as much as possible before extrusion of the laminate. (The real extruder takes an eight layer inflow and splits it into sixteen layers.) The mesh for this geometry is given in figure 17. This is a relatively coarse mesh that can be run on a single processor. It contains 9276 hexahedral elements, 12040 nodes, and 84,280 total degrees of freedom.

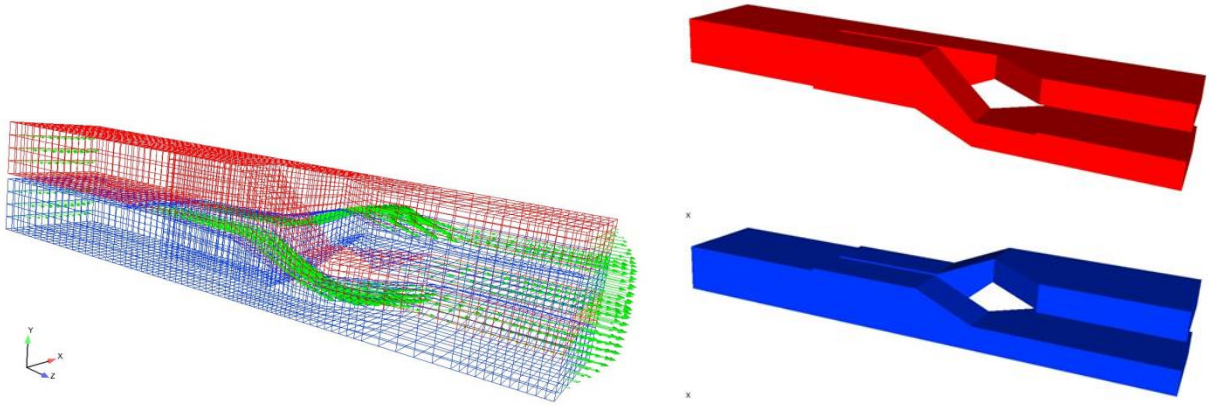

Figure 17: Coextruder mesh for initial multiplication creating a four-layered structure by splitting and restacking a two-layered one. Velocity vectors on mesh (left) show acceleration and redirection of fluid through the splitter. The view on the right shows a break out of the two fluids to more clearly see the splitter design.

The top and bottom fluid are shown separately to understand the configuration of the splitter as it cuts the flow vertically and then restacks the fluids to double the number of layers. The polymer must accelerate and change direction in the splitter, which is a combination that can lead to instabilities, especially for non-Newtonian fluids. The flow splitters and duct wall all have no slip boundary conditions. The free surface exists between red and blue fluid downstream from the splitter, where surface tension and the kinematic condition are applied assuming that the polymer matrices are different for the conductive and dielectric materials and there is some interfacial tension. The inflow boundaries have constant applied pressure. Boundary conditions must be applied to momentum equations and mesh equations and there are sixteen different side sets in the mesh to represent the geometric complexity involved. For moving mesh simulations in GOMA, rotation conditions must be applied by hand for any boundary condition that is expressed in a normal, tangential fashion such as the kinematic condition or slip velocity conditions. This makes for very complex input files.

Because we were doing scoping calculations before the materials had been selected, we tried to get a range for possible material properties for our simulations. For our initial material selection, we assumed nickel particles in a polystyrene base. Oscillatory rheometry for the base polystyrene at different temperatures is given in figure 18. Also given in figure 18 is the response at 210^{o}C for different amounts of filler. Viscosity measured from oscillatory rheometers gives us a qualitative idea of the fluid behavior, but is not quantitative as shear rheology would be.

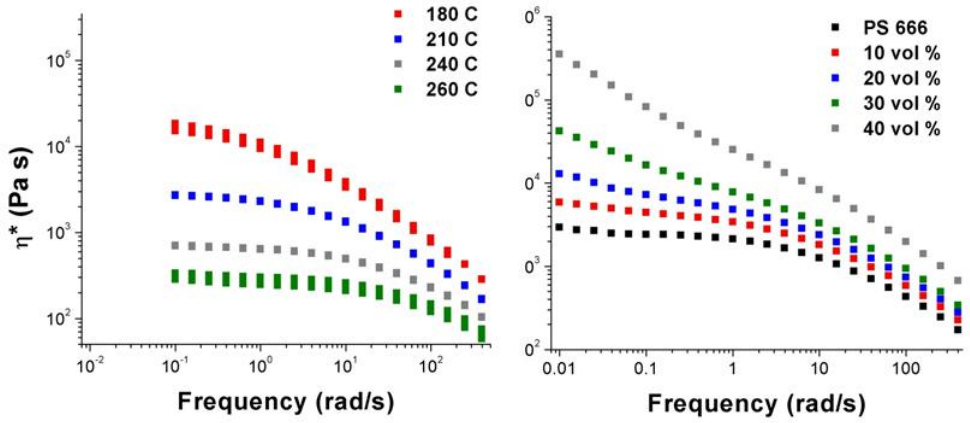

Figure 18: Viscosity of neat polystyrene resin as a function of temperature from 180^{o}C–260^{o}C (left) and as a function of 200nm nickel particle content from 10-40 vol% at 210^{o}C (right).

From the rheological measurements, we can infer that the polystyrene is shear thinning and temperature dependent, with the viscosity dropping as the temperature is increased. The filler increases the viscosity of the composite system, and this increase is related to the volume fraction of particles. It is also more pronounced in the low shear-rate regime, as the zero shear-rate viscosity increases more than the high shear-rate viscosity. The density is assumed to range from roughly 1 g/cc, which is the density for neat polystyrene, to 5 g/cc for a filled polymer. From running the coextruder, we estimate a velocity at outflow of 0.25-4cm/s. The interfacial

tension is estimated to be negligible for cases where we use the same polymer matrix for both conductive and dielectric phases, and as 20 dyne/cm for dissimilar polymers such as polystyrene/polyethylene coextrusion. These characteristic properties and processing parameters are given in Table 1.

Table 3. **Characteristic properties and processing parameters for modeling**

Property	**Range**
Viscosity	10^3-10^5 Pa-s
Density	1 -5 g/cc
Characteristic velocity	0.25-4 cm/s
Interfacial tension	0-50 dyne/cm

4.3 Results for ALE Modeling of the Splitter

We also investigated the flow splitter section of the coextruder where the eight-layer structure is split and restacked to produce a sixteen-layer structure. In this section, instabilities are often seen and quieting regions are often placed after these flow splitters to produce a more axial, and stable flow pattern. Here we have an idealized flow splitter where a two-layer structure is split and restacked to form a four-layer structure. Results from these simulations should be applicable to the real coextruder and its sixteen-layer structure.

We first ran a simulation with the same fluid properties for both layers, but with a kinematic condition on the interface. The kinematic condition does not allow mixing between the two fluids. This case gives us insights into how the geometry affects the shape of the layers without clouding the results with differences in material properties. Results for this case are given in Figure 19.

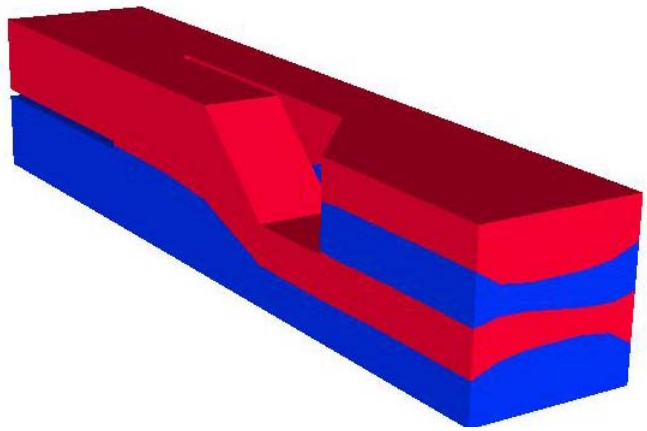

Figure 19: Simulation results for a flow splitter mold containing a red and a blue fluid. The properties are identical for both fluids: The viscosity is 10,000 Poise and the density is 1 g/cc. Because of the design of the splitter, the layers at the out flow are not uniform in thickness even for the same material properties in both fluids. The interfacial tension between layers is assumed to be 45 dyne/cm.

Because of the splitter design, the layers at the outflow are not uniform in thickness, nor do they have a flat meniscus between lamellae. The design of the splitter could be improved in future, perhaps by using an inverse analysis method that keeps the layers flat and changes the splitter geometry to be consistent with that interface shape.

From this initial condition, we use parameter continuation to slowly increase the viscosity of the red phase while keeping the viscosity of the blue phase constant at 10,000 Poise. The interfacial tension between layers is assumed to be a constant value of 45dyne/cm. We were able to run the problem until the mesh became too corrupt to continue. This occurred at a red phase viscosity of 64,000 Poise or a viscosity ratio of 6.4. The results for this viscosity ratio are shown in figure 20. We can see that the red fluid sandwiched between the two layers of blue fluid has thinned down to about a third of its initial size, while the top red layer that is in contact with the die has stayed close to its initial size.

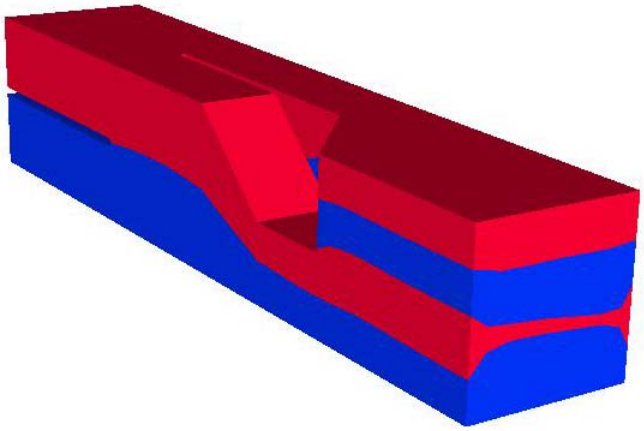

Figure 20: Simulation results for parameter continuation of the red phase viscosity from its initial value of 10,000 Poise to 64,000 Poise, where the mesh becomes too distorted to support further simulations. The blue phase is held constant at 10,000 Poise and the density of both phases is 1 g/cc.

We also investigated increasing the pressure in the red phase, while keeping the properties of the both fluid the same at 10,000 Poise and 1 g/cc. Again, we used parameter continuation to run one steady state simulation to another with a higher inflow pressure, using the low pressure as an initial condition for the higher pressure. From these simulations, it was found that the red phase pressure could be roughly 1.8 times the blue phase pressure at which time the mesh became too deformed to support further calculations and the outflow meniscus had lost its lamellar structure. At this pressure, the red layers are almost touching, but cannot actually touch because ALE meshes cannot handle topological change without remeshing.

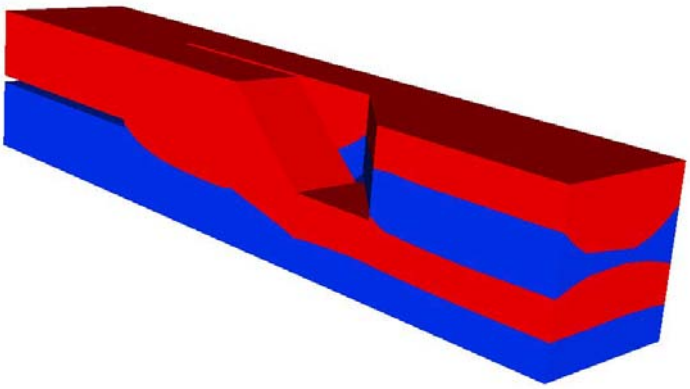

Figure 21: Simulation results for parameter continuation of the red phase inflow pressure from its initial value of 10,000 dyne/cm^2 to 17,650 dyne/cm^2, where the mesh becomes too distorted to support further simulations. The red and blue phase properties are held constant at 10,000 Poise and 1 g/cc. The interfacial tension between layers is assumed to be 45 dyne/cm.

4.4 Results for Level Set Modeling of the Splitter and Comparison to ALE Modeling

Because our simulations using the ALE method would run until the mesh became too distorted for further simulations to converge as we continued in parameter space, we decided to investigate using the level set method. The level set method, being an Eulerian method, can better handle topological changes such as the merging of layers. We first compared the results from the ALE base case to the level set for the same parameters. Results for this comparison are given in Figure 22.

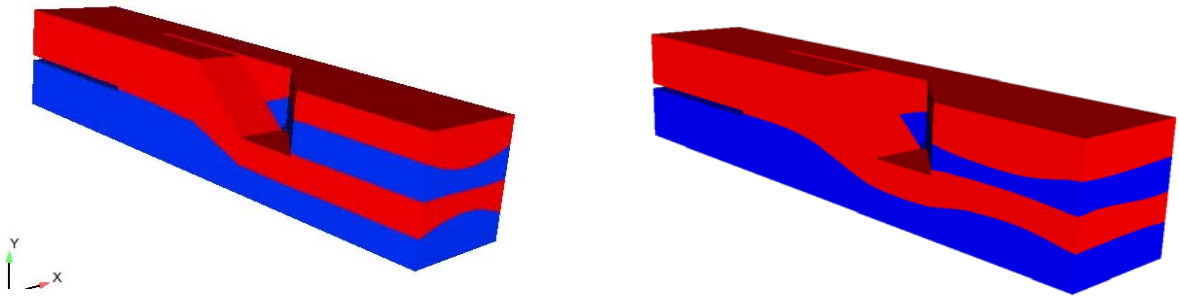

Figure 22: Comparison of ALE result (left) to level set result (right) for the same properties and inflow pressure (10,000 dyne/cm^2). The red and blue phase properties are equal at 10,000 Poise and 1 g/cc. The interfacial tension between layers is assumed to be 45 dyne/cm.

From figure 22 we can see that the steady ALE simulation has very little movement of the fluid-fluid interfaces at the wall, since it clearly obeys the no slip condition applied. The inherently transient nature of the level set simulation introduces some slip at the wall, even when no slip is

applied, since the interface location evolves in time. The level set simulations show more motion at the wall than the ALE simulation and result in more even and well-behaved layers.

We wanted to determine which boundary condition was more appropriate: slip, where there is some fluid motion at the solid-fluid interface, or no slip, where the velocity is identically zero. To this end, we undertook a validation experiment to look at materials with the same density and viscosity and run at the same flow rate. To differentiate the two polymers, we added 3vol% carbon black to create a black material and 3vol% titanium dioxide to the other layer, to create a white material. This was an amount suitable to change the color of the polymer without affecting their physical properties. Results from the validation experiment are given in figure 23.

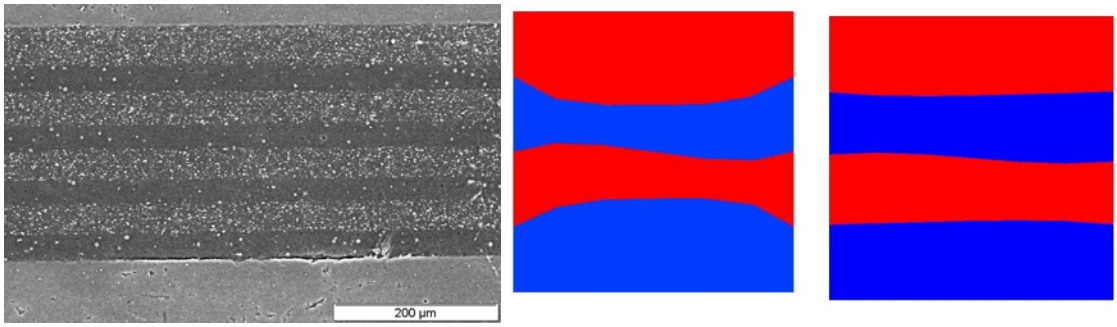

Figure 23: Comparison of black and white experiment SEM (left) to ALE result (middle) to level set result (right) for the same properties and inflow pressure (10,000 dyne/cm^2). The red and blue phase properties are equal at 10,000 Poise and 1 g/cc. The interfacial tension between layers is assumed to be 45 dyne/cm.

From this validation experiment, it was determined that some slip does occur at the walls during coextrusion and that either running transient, e.g. for a level set method, or using a Navier slip boundary condition ALE simulations is preferable to steady simulations with no slip.

4.5 Results for Level Set Modeling of the Splitter for Different Viscosity Ratios

We used the level set method to investigate property ratios and processing parameters that we could reach with moving mesh methods. Figure 23 shows results for an equal order, but higher inflow pressure (100,000 dyne/cm^2) and equivalent properties. For this inflow pressure, we see distortion of the red fluid sandwiched between the two layers of blue fluid. If we increase the viscosity ratio between fluids by making the viscosity of the red fluid 10 times that of the blue fluid, we see that we get total encapsulation of the red fluid by the blue and loss of the layered structure as the two blue layers coalesce.

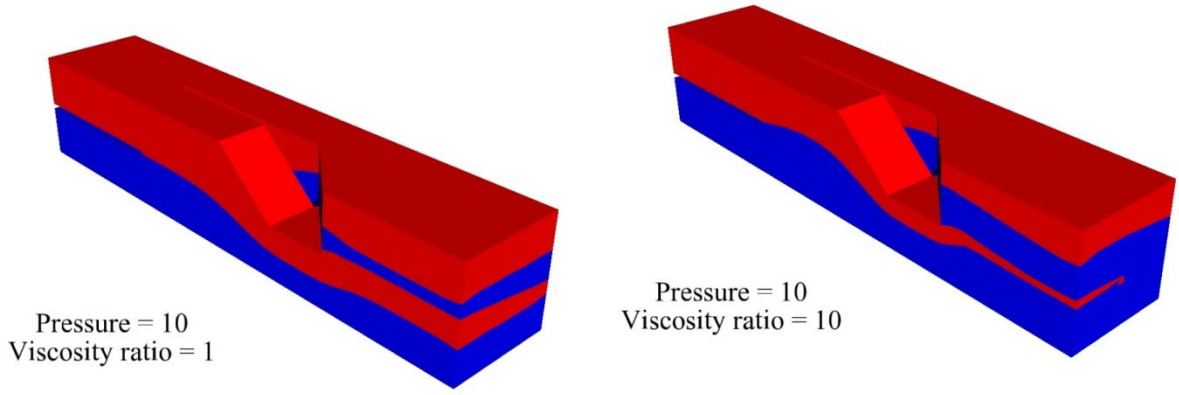

Figure 24: Comparison of level set results for the same properties and inflow pressure (100,000 dyne/cm^2) (right) with level set results for red phase viscosity of 100,000 Poise with blue phase viscosity at 10,000 Poise (left). Both densities are held constant at 1 g/cc. The interfacial tension between layers is assumed to be 45 dyne/cm.

5 RESULTS USING CAPACITOR MATERIAL PROPERTIES

5.1 Rheology of Capacitor Materials

Late in the project, we were able to produce and compound enough material using the large twin screw extruder to enable us to measure the rheology of the novel conductive polymer. The conductive material is a mixture of 12vol% Ni particles and 28vol% of a low melting point eutectic (The eutectic, Cerrotru, is 58% bismuth and 42% tin, a commercial material from McMaster-Carr for soldering) in a polystyrene matrix (Dow Styron 666D). This material is designed to have the eutectic as liquid droplets dispersed in the polymer with the Ni particles added to help disperse the low viscosity liquid and produce a relatively low viscosity mixture (when compared to a composite with the same metal volume fraction and all solid particles) and a processible material for capacitor coextrusion. An SEM of the conductive material is shown in figure 24. A parallel plate rheometer was used to understand the low shear-rate behavior and a capillary rheometer was used to understand the high shear-rate behavior of the conductive material at 225^{o}C, thought to be the average temperature seen in the coextruder.

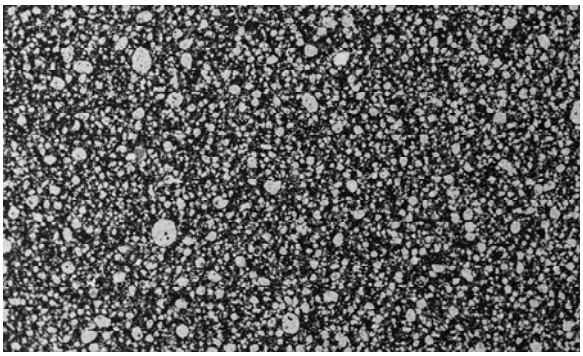

Figure 25: SEM showing microstructure of well-mixed Ni-Eu-PS composite.

For the dielectric phase, we chose to use 20 vol% Barium Titanate ($BaTiO_3$) powder dispersed in polystyrene. $BaTiO_3$ is a ferroelectric ceramic that has a high dielectric constant and is used in its pure state as a dielectric material for traditional capacitors. An SEM of the dielectric material is shown in figure 26.

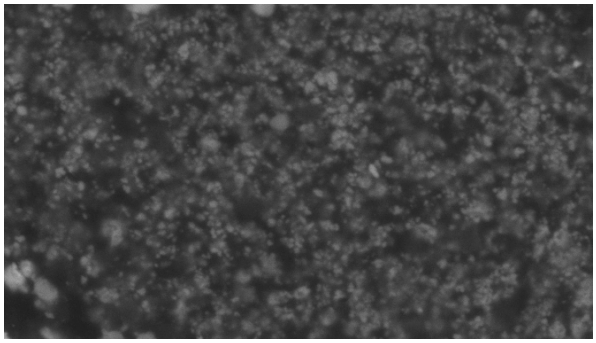

Figure 26: SEM of Barium Titanate at 1000x

Here the addition of the $BaTiO_3$ (BT) not only improves the dielectric properties of the filled-polymer, but should make the density and viscosity of the dielectric phase a closer match to the Ni-Eu-PS composite. The rheology of the neat polystyrene (PS), Ni-Eu-PS composite material and $BaTiO_3$ -PS composite are shown in figure 27. The filled-polymers show a similar shear-thinning behavior as the polystyrene matrix, but have a more dramatic increase in viscosity at low shear-rate. From the data, we can see that the effect of the filler is more pronounced at low-shear rates and less obvious at high-shear rates. The $BaTiO_3$ filler increases the low shear-rate viscosity by a factor of ten, while the Ni-Eu filler increases the low shear-rate viscosity by a factor of a hundred. This is significant since the coextruder is estimated to run at shear rate of 60-100 1/s or below. The high shear-rate viscosity increases from the pure polymer by roughly a factor of two for the $BaTiO_3$ and a factor of three for the Ni-Eu-PS. It is possible that there are interactions between the long chain polystyrene molecules and the particles or droplets in the composite materials and a weak network is formed at low shear rate that is then broken up at higher rates.

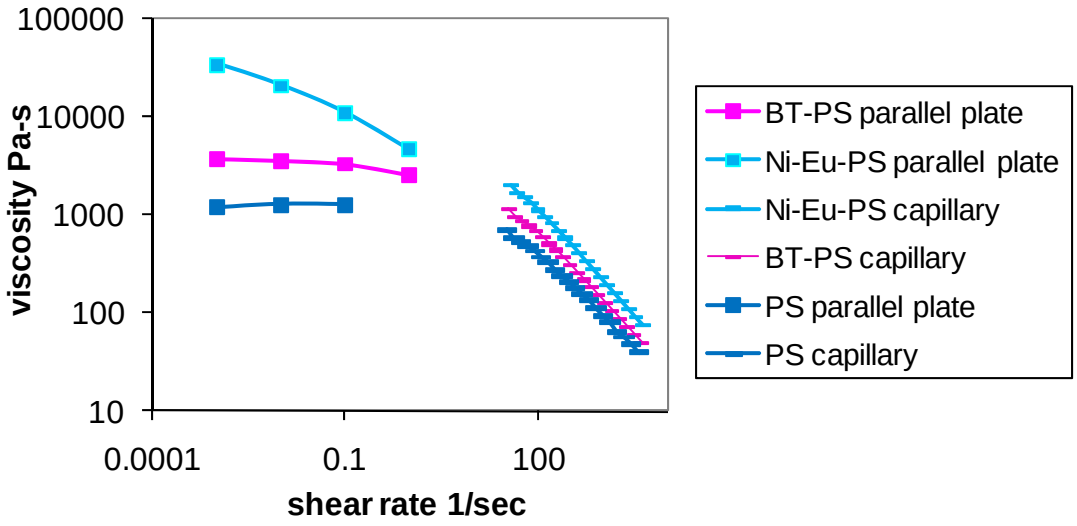

Figure 27: Parallel plate and capillary rheology for neat polystyrene (PS), BT-PS filled polymer, and Ni-Eu-PS filled polymer at 225°C.

It is clear from the data, that the low shear rate behavior for the conductive material is more solid-like than fluid-like given that the zero shear-rate viscosity is 40,000 Pa-s (for reference, the viscosity of water at room temperature is 0.001 Pa-s). We have chosen the conductive material to have only 12vol% solid Nickel particles and 28% low melting point eutectic in high molecular-weight polystyrene. The melting temperature of the eutectic is on the order of 138°C, which means that at processing temperature of 225°C it forms an emulsion in the polystyrene with the nickel particles acting as mixing beads and helping to keep the immiscible eutectic from phase segregating from the polymer matrix and keeping the droplet size low. We assumed that the material would be more processible than a traditional particle-filled polymer system at the percolation threshold for conduction, but from the rheology we can see that the material is not

that well-behaved and that it would be a good idea to find a lower viscosity, and less shear-thinning polymer matrix on which to base our composite on. We may also be able to reduce the viscosity of the composite by adding processing/dispersal aids such as surfactants; this idea will be considered for future materials.

A Carreau-Yasuda model [Bird et al., 1987] was used to fit both the parallel plate and capillary data and is shown in figure 28. This model is also suitable for using in finite element simulations as it is well-behave at zero-shear rates compared to other similar models such as a Power Law model. The fit has more of a zero-shear plateau than the data, but was deemed acceptable for the numerical simulations.

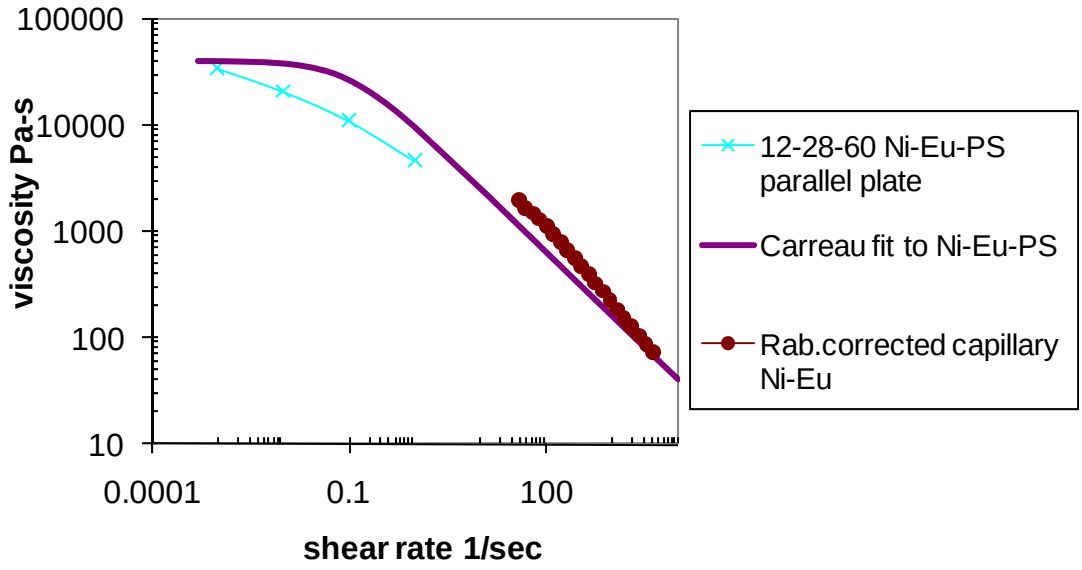

Figure 28: Low shear-rate parallel plate rheometry (blue) and high shear-rate capillary rheometry (red) data for 12vol% Ni, 28vol% Eutectic, and 60vol% polystyrene conductive polymer at 225°C. The rheology was fit to a Carreau model that spans both set of data (purple).

Similar data was collected for the dielectric phase, of 20vol% $BaTiO_3$ in 80vol% polystyrene at 225°C (figure 29). The dielectric material rheology was fit to a Carreau-Yasuda model that spans both the low shear-rate parallel plate rheometer data and the high shear-rate capillary rheometer data.

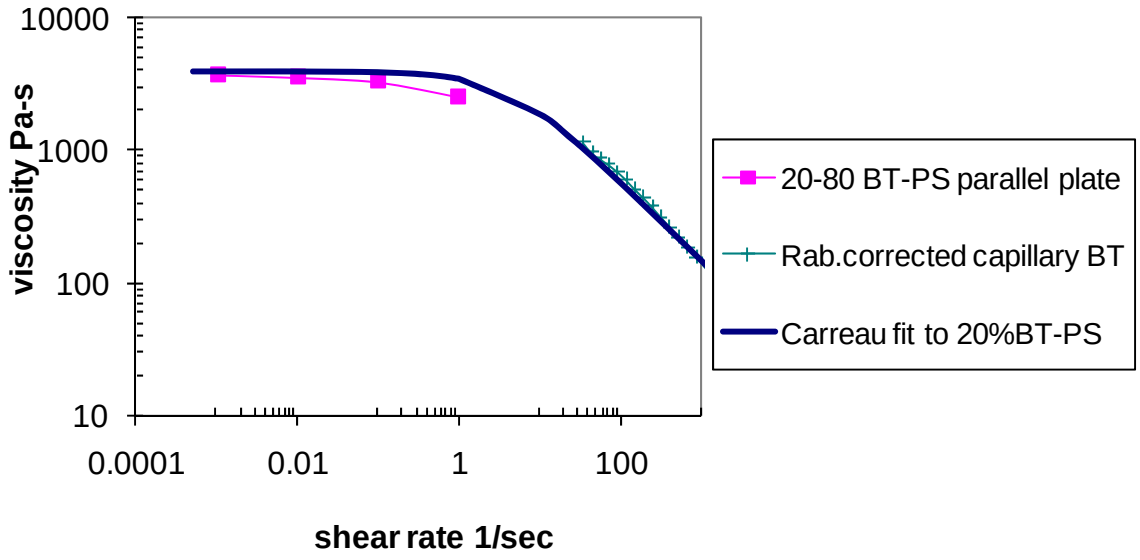

Figure 29: Low shear-rate parallel plate rheometry (pink) and high shear-rate capillary rheometry (turquoise) data for 20vol% $BaTiO_2$ and 80vol% polystyrene conductive polymer at 225°C. The rheology was fit to a Carreau model that spans both set of data (blue).

The rheology of the dielectric material is similar in shape and slope of the power-law regime to the conductive phase, but has an order of magnitude lower zero shear-rate viscosity of 4,000 Pa-s. Table IV summarized the fit to the Carreau model for both filled-polymers. See equation (10) for the form of the Carreau-Yasuda model.

Table IV: Density and Parameters for Carreau-Yasuda fit for conductive and dielectric filled-polymer composite materials

Property	Ni-Eu-PS material	$BaTiO_2$ –PS material
Zero shear-rate viscosity, η_0	40,000 Pa-s	4,000 Pa-s
Infinite shear-rate viscosity, η_∞	1 Pa-s	1 Pa-s
Time Constant, λ	1.0 s	0.25 s
Power-law exponent, n	0.4	0.4
Transition exponent, a	1.0	1.0
Density, ρ	4.09 g/cm^3	2.06 g/cm^3

Comparison to theory

Figure 30 shows a theoretical viscosity rise for a suspension of solid spheres as a function of volume fraction [Krieger and Dougherty, 1957] and an emulsion of droplets of the same volume fraction for two different emulsion correlations, Taylor-Mooney [Taylor, 1934; Mooney, 1961] and Frankel-Acrivos [Frankel and Acrivos, 1970]. From figure 27, we can see that a theoretical viscosity increase for a 40%vol particles composite similar to our Ni-Eu-PS material, will be less than a factor of 3 from the neat polymer, while we are seeing a factor of 40 increase in the zero-shear rate viscosity.

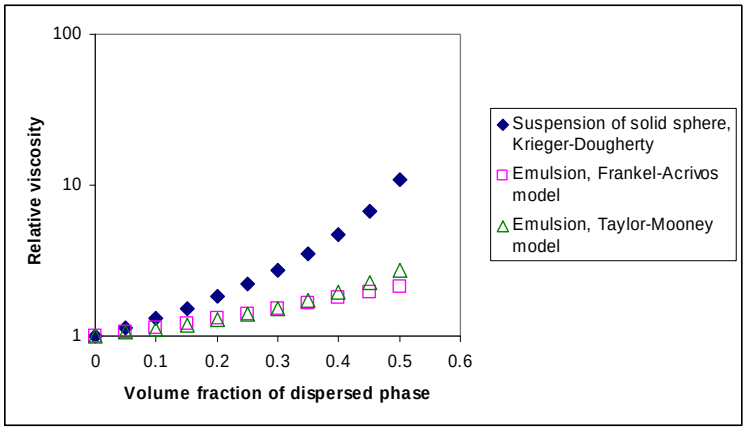

Figure 30: Relative viscosity versus volume fraction for a suspension of particles and an emulsion of droplets.

We can see this divergence of the data from the theoretical predictions even more clearly from figure 30, which shows Farris theory for the Ni-Eu-PS conducting polymer and Krieger-Doherty theory for the $BaTiO_3$-PS dielectric polymer. Theoretical viscosities were determined and are given below. The Krieger-Dougherty correlation can be used to predict the viscosity of a suspension of $BaTiO_3$ in PS matrix. This yields a viscosity η_s, where we are assuming noncolloidal spheres, which are greater than one micron in size:

$$\eta_{PS-BT} / \eta_{PS} = (1-\varphi / \varphi_{\max})^{-2.5\varphi_{\max}} \qquad (25)$$

If we treat the mixture as a suspension of Ni particles in a continuum with the viscosity of an emulsion of the eutectic (Eu) droplets along in the polystyrene, we can use Farris theory to predict the viscosity of the three-phase composite, Farris theory gives an estimate of a mixture of particles [Farris, 1958]. For a mixture of 12% Ni suspended particles (Krieger-Dougherty) in emulsion of 28% eutectic droplets in polystyrene (Taylor-Mooney) we obtain:

$$\eta_{PS-Eu-Ni} = \eta_{PS-Eu}(1-\varphi / \varphi_{\max})^{-2.5\varphi_{\max}}$$
$$\eta_{PS-Eu} = \exp(\frac{\varphi}{1-\varphi}) \qquad . \qquad (26)$$

Results comparing the theory to experimental data are shown in figure 31. From this figure, we can see that the theory works well at high shear-rates, but is quite off from the rheology at low shear rates where the material looks almost jammed.

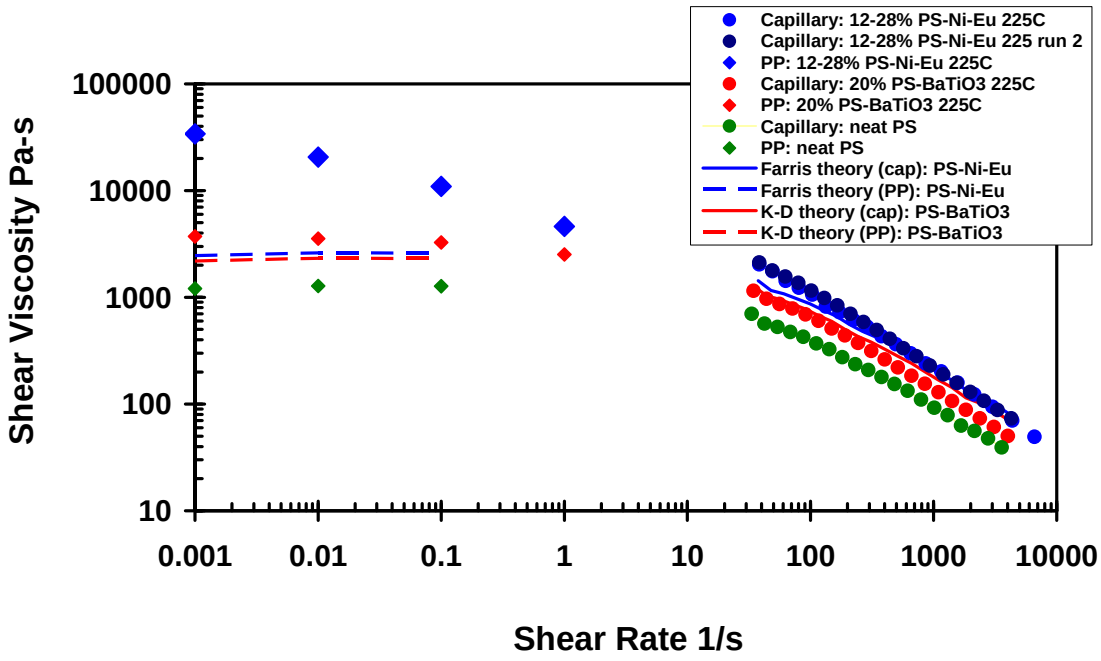

Figure 31: Rheology compared to theory for suspensions and emulsions

5.2 Results for Level Set Modeling of the Splitter

As we came closer to a material down selection for the conductive and dielectric, we wanted to understand how the stability of the flow would be affected by both dissimilar densities and viscosities. For this case, we use a red phase viscosity of 25,000 Poise and density of 4.09g/cc to represent the conductive polymer, which is a mixture of 12vol% Ni particles and 28vol% eutectic in polystyrene. The blue phase viscosity was 15,000 Poise and the density of 2.06g/cc to represent the dielectric, which is a composite of 20% barium titanate ceramic particles in polystyrene. Both filled-polymer systems are shear-thinning, but we assume they are Newtonian for this study, and estimate their viscosities from preliminary data and a shear-rate estimate of 60Hz. Because the polymer matrix is the same in both phases, we assume that there is no interfacial tension between the phases. The results from this test case are given in figure 32.

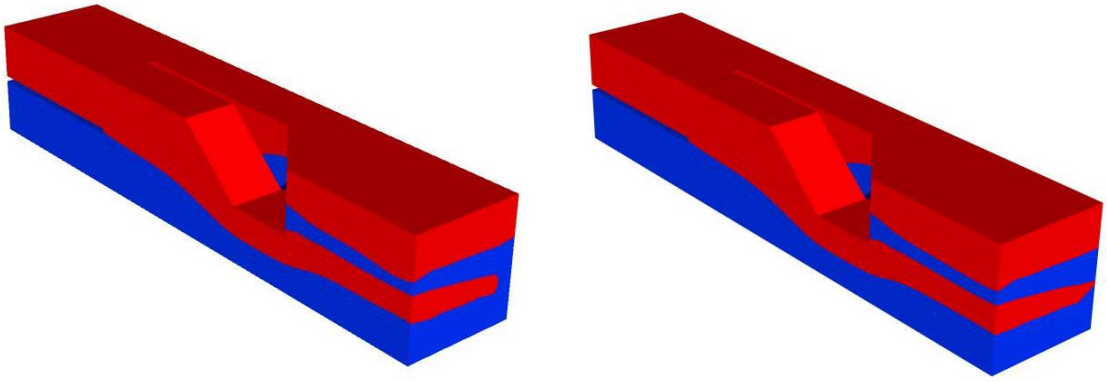

Figure 32: Level set simulations for the estimated properties for the conductive red phase (25,0000 Poise, 4.09g/cc) and dielectric blue material (15,0000 Poise, 2.06g/cc). The inflow velocity is 5 cm/s. The picture on the left shows the simulation at an early time when the bottom red sheet breaks. The picture on the right shows it reforming at later times, which ends up being the steady profile.

From figure 32, we can see that the combination of mismatched viscosity (ratio = 1.667) and mismatched density (ratio = 1.99) results in problems in the splitter where the conductive red fluid can become encapsulated by the lower viscosity blue dielectric fluid, and the bottom red layer breaks and then reforms in the steady solution. Oscillations occur in the solution where we see waves in the bottom meniscus reminiscent of Rayleigh-Taylor instabilities. Because we are interested in short turn-around-times for the simulation, a relatively coarse mesh was used. In future, we recommend revisiting these simulations with a finer mesh.

5.3 3D Free Surface Flow in the Drawdown Region

Our first efforts at coextruding a capacitor involved using the coextruder without splitters to make an eight layer structure from the four inflows of dielectric material and four inflows of the conductive material. Once a layered structure is formed, two drawdown regions take the cross-section of the capacitor from square to a thin tape, which is then drawn down even further as it is extruded and squeezed between chilled rollers. The first drawdown maintains the area of the cross-sectional area of die, while the second drawdown decreases the area by half, requiring acceleration of the fluid.

To better understand the flow and possible instabilities that occur without the splitter, we created a mesh that includes the two draw downs, but ignores the inflow region and the free surface extrudate flow to the chilled rollers. Here we use a level set method with equations averaging in ARIA to better understand the multi-material instabilities possible in the drawdown region. The mesh for this problem is shown in figure 33. The mesh has 35629 nodes, 31200 elements, and 142516 unknowns. The boundary conditions include a plug flow inflow, open flow outflow, and no slip on solid boundaries. Gravitational effects are important, so the open flow out flow boundary condition was crucial to obtaining well-behaved solutions.

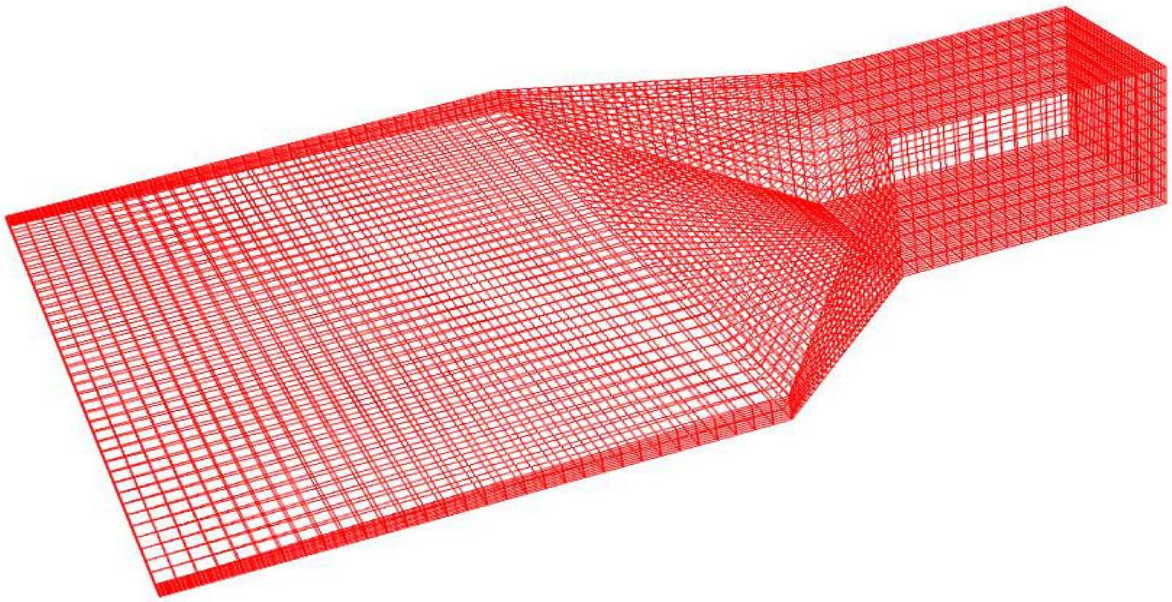

Figure 33: Mesh for draw down region that takes the coextruded material from a square cross-section down to a tape. The flow goes from right to left with the initial cross-section being 1.27cm by 1.27cm drawdown to 5.08cm by 0.2cm in 2.54cm. The second drawdown is more gradual over 3.81cm to 5.08cm by 0.1cm.

5.3.1 Newtonian Rheology: Denser More Viscous Fluid over Less Dense, Less Viscous Fluid

We first tried running the mesh shown above with a Newtonian description of the rheology. We assumed that there were only two fluids in the coextruder, with the initial condition being half heavy fluid in the upper part of the domain and light, less viscous fluid in the bottom of the domain. The initial conditions are shown in figure 34.

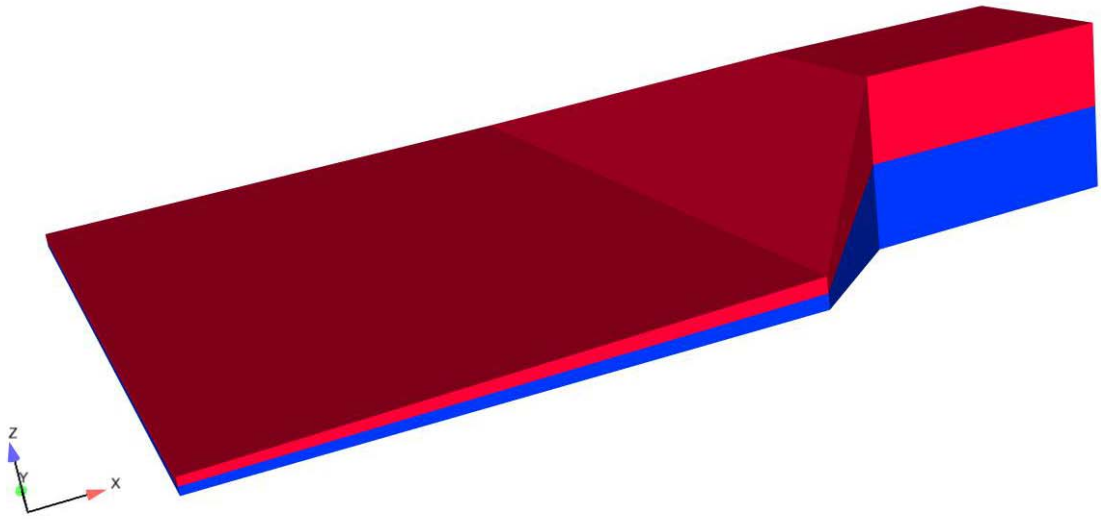

Figure 34: Initial condition for coextrusion simulations of draw down region.

Since the fluid is shear-thinning and there is no single Newtonian viscosity that represents the material, we chose the zero shear-rate viscosity as the characteristic viscosity for the flow. We could also chose the viscosity at the average shear rate in the coextruder, but this seem to be an extreme test of the method since the viscosity mismatch is so large. Because these viscosities are so large, the matrix becomes poorly scaled and the nondimensionalization was crucial to improving the condition number of the matrix enough to solve the problem. Since we have both a viscosity and density mismatch, we felt that instabilities would be present in the flow, but did not know if our numerical method would be accurate enough to capture it. Figure 35 shows the results for coextruding two Newtonian fluids with a viscosity and density mismatch and the heavier, more viscous fluid on top.

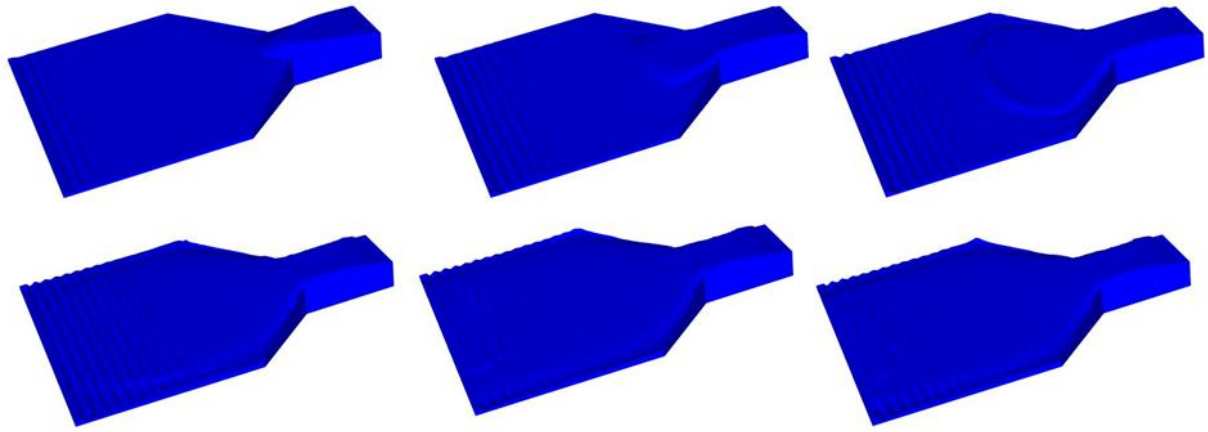

Figure 35: Bottom fluid free surface profile for Newtonian properties (40,000 Poise, 2.06g/cc) as a function of time at 0.5s, 1.0s, 2.0s, 5s, 7s, 10s: The top fluid has 10 time the viscosity of the bottom fluid and twice the density (400,000 Poise, 4.09g/cc). A barring instability is seen toward the exit of the die and pooling of the light, less dense fluid is seen as the fluid goes into the first draw down section. By 10s the fluid has reached an equilibrium profile exhibiting barring at the edges of the flow and a smooth meniscus in the center of the die.

From figure 35, we see the development of lower fluid meniscus as a function of time. This shows a barring instability at the outflow and pooling of the fluid as it enters the first draw down region. By 10s the fluid has reached an equilibrium profile exhibiting barring at the edges of the flow and a smooth meniscus in the center of the die. The interface show some encapsulation of the high viscosity fluid by the low viscosity fluid and a barring instability at the edges of the die. Both of these effects imply that the system will not be well behaved. This poor behavior would likely be magnified if we included all eight layers in our simulations.

5.3.2 Shear-thinning Rheology: Denser More Viscous Fluid over Less Dense, Less Viscous Fluid

We also did simulations in the drawdown geometry using the Carreau fits for the conductive and dielectric materials given in Table IV. In these simulations, the viscosity changes with shear-rate similarly to the experimental data. Because the zero-shear rate viscosities of the conductive and dielectric phases are so high, the problem was numerically poorly conditioned. To improve the

condition number of the discretized equations, we solve the problem in dimensionless form as discussed in the theory section. The nondimensionalization results in various dimensionless numbers and property ratios that can help characterize the flow and the differences between the fluids. Here *v* is defined as a characteristic inflow velocity (1cm/s), d is the inflow height of 1cm, g is the gravitational acceleration of 980 cm/s, σ is the interfacial tension between fluids assumed to be 0 dyne/cm since the fluids have the same continuous phase (the interfacial condition at the level set zero keeps the materials from mixing), densities of the heavy and light fluids are taken from Table II with the zero-shear rate viscosity of the light fluid used as the characteristic viscosity. This value also modifies the infinite shear-rate viscosities of both fluids. Using therse values, the dimensionless numbers from equation (5) are:

$$\begin{aligned}
&\mathrm{Re} = \frac{\rho_l v d}{\eta_l} = 5.15e-5 \\
&\frac{\mathrm{Re}}{Fr} = \frac{\eta_h v g}{\rho_h d^2} = .0505 \\
&Ca = \frac{\eta_l v}{\sigma} = \infty \\
&\beta = \frac{\eta_{0h}}{\eta_{0l}} = 10 \\
&\beta_1 = \frac{\eta_{\infty h}}{\eta_{0l}} = 0.00025 \\
&\beta_2 = \frac{\eta_{\infty l}}{\eta_{0l}} = 0.00025 \\
&\Gamma = \frac{\rho_h}{\rho_l} = 1.985
\end{aligned} \quad . \qquad (27)$$

Results using the dimensionless shear-thinning rheological model are shown in figure 36 and 37 as the flow field develops with time for the bottom fluid and top fluid respectively. The initial condition is the top half of the die half-filled with conductive material and the bottom half-filled of the mold filled with dielectric material.

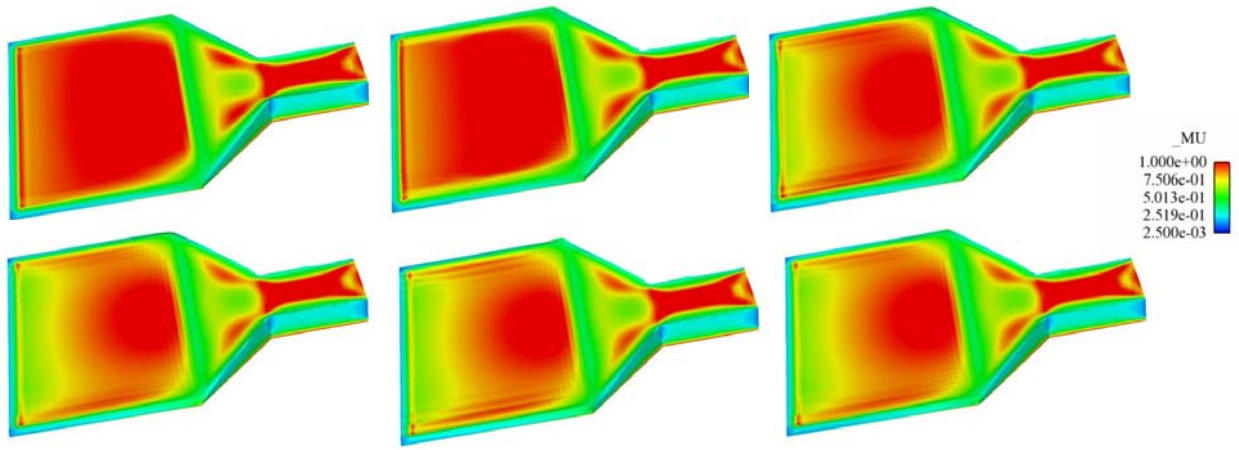

Figure 36: Lower fluid meniscus and evolving viscosity with time at 0.5s, 1.0s, 2.0s, (top row from left to right) 5s, 7s, 10s (bottom row, from left to right). A ribbing instability is seen at 7.0s, but starts to damp out at later times. The simulations never reach steady state, but oscillate between two states with the shear surface jumping forward and backwards near the outflow).

From figure 36 we can see the evolution of the dimensionless viscosity as the shear field develops over time. It starts out somewhat homogenous at 0.5s with a high dimensionless viscosity of 1.0 in most of the domain, except at the walls where it shear-thins to a low value of the viscosity. A ribbing instability is seen at 2.0s and then disappears only to reappear at 7.0s. By 10s the ribbing instability has damped out, but the solution never reaches steady state. Instead it jumps between two semi-stable states with different flow fields and viscosity distributions. The dynamic effects of this are easier to see in a movie made from these images. As expected the viscosity stays highest at the center of the mold away from the walls and before the drawdown region. Once it enters the drawdown the viscosity shear-thins down to a low value.

Figure 37 shows the viscosity and the meniscus of the more viscous upper fluid as a function of time. This is the negative imprint of the lower meniscus shown in figure 36 and show the same evolution to a time-dependent state. The viscosity, on average, is higher in the upper fluid, though it is also shear-thinning.

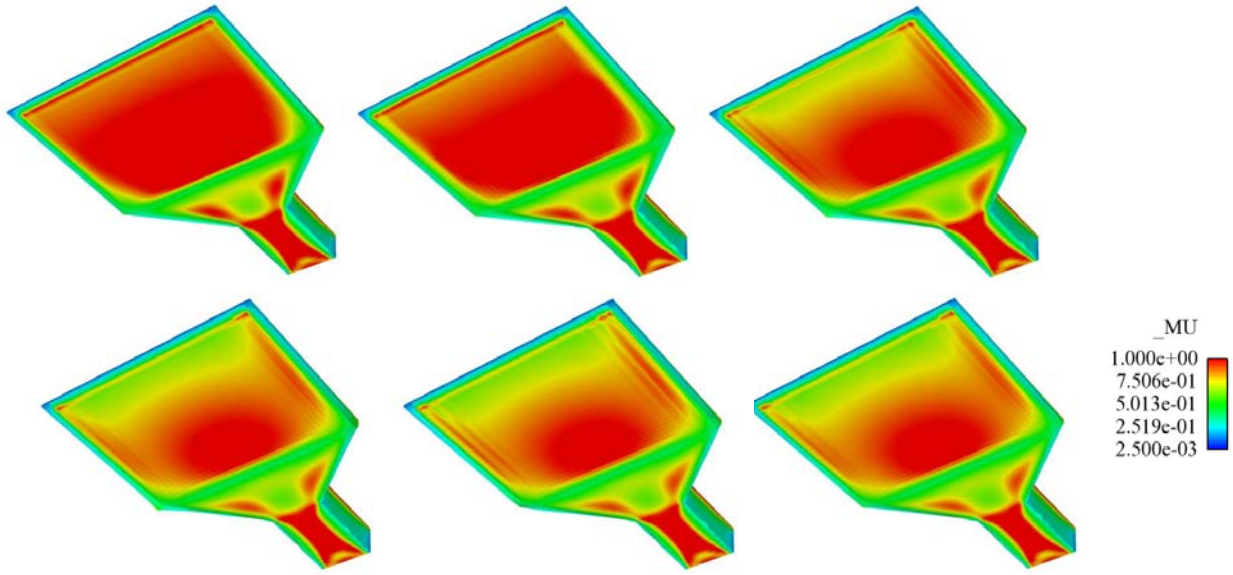

Figure 37: Upper fluid meniscus and evolving viscosity with time at 0.5s, 1.0s, 2.0s, 5s, 7s, and 10s. A ribbing instability is seen at 7.0s, but starts to damp out at later times. The simulations never reach steady state, but oscillate between two states with the shear surface jumping forward and backwards near the outflow.

The viscosity in the fluid can be seen more clearly from axial slices of the dimensionless viscosity as it travels down the mold, which is shown in Figure 38, at the final time of 27.9s.

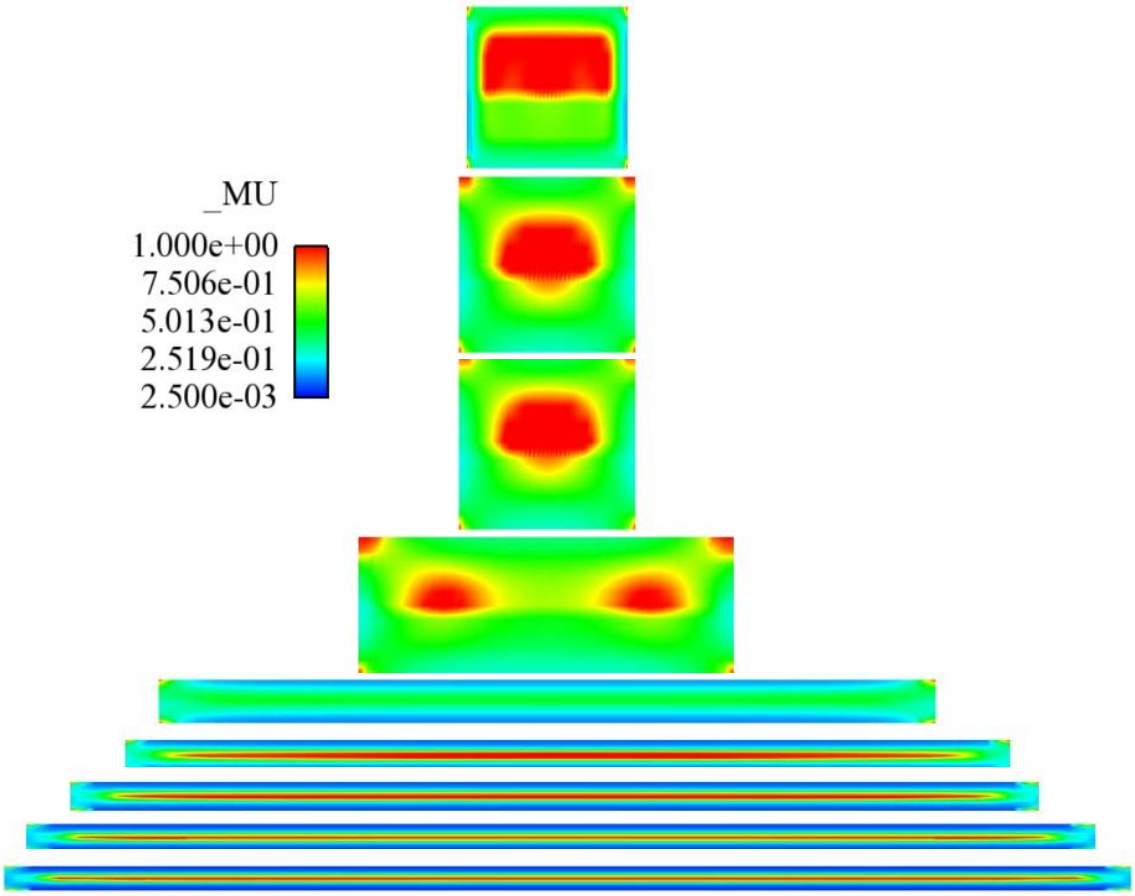

Figure 38: Axial slices of the viscosity as it moves down the mold from the entrance to the drawdown region at 27.9s. (Inflow is at the top of the image and we move axially down the extruder.) The viscosity of the top fluid is higher than the bottom fluid based on the rheology of the real materials.

The more viscous fluid comes in at a higher viscosity indicated by the red color at the top of the mold. It shear thins as the mold narrows through the coat hanger section of the die and then shear-thins further as it is extruded through the drawdown region, with high viscosity regions exiting at the center of the die near the interface between the two fluids. High viscosity regions also exist in the corners of the mold, which could also lead to processing difficulties.

Figure 39 shows the outflow profile and fluid-fluid interface as it evolves over time. The initial meniscus starts out flat at the initial condition and then evolves to be somewhat wavy. The instability starts at the edges of the coextruder and then works its way in slightly leaving thicker regions of the blue fluid at the edges and thinner regions in the center. This is not an optimal profile, since for a coextruded capacitor to work optimally we would hope to have uniform thickness of the layers.

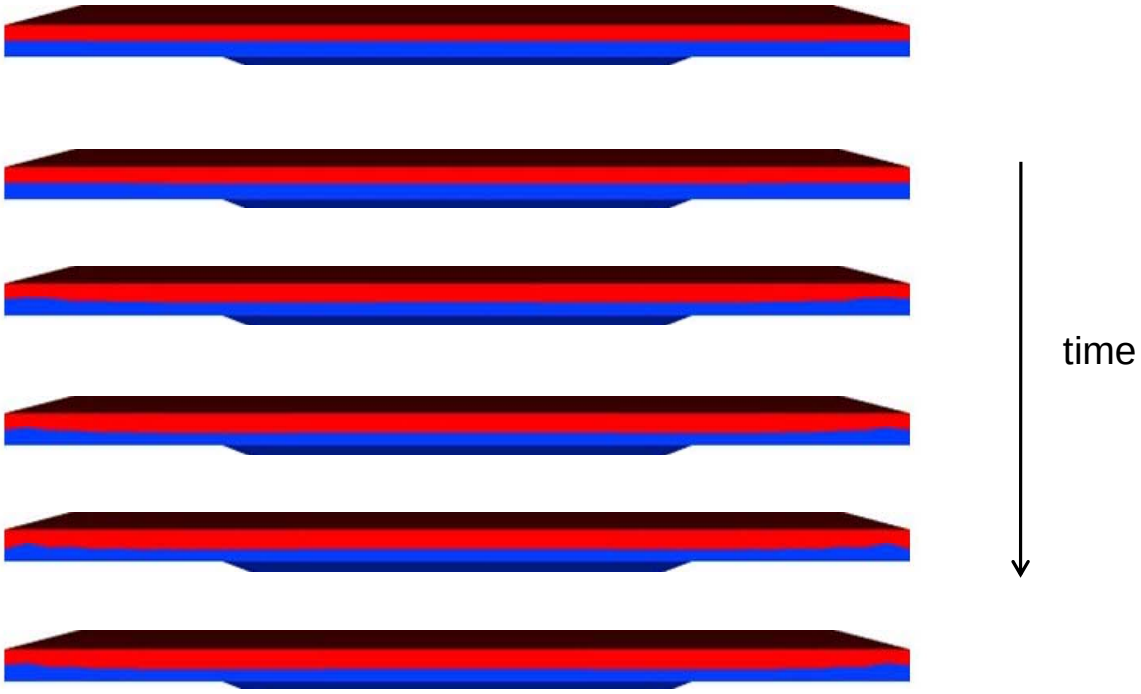

Figure 39: Outflow profile as a function of time for 0.5s, 1.0s, 2.0s, 5s, 7s, 10s.

The final profile at 29.7s (Figure 39) shows that the instability at the edges have died out, but the blue fluid remains thinner in the center than at the edges.

Figure 40: Outflow profile at long times (t=29.7s).

We also examined the case where there was interfacial tension between the two fluids of σ=20 dyne/cm. For this case, the capillary number, Ca, is 889, which is still large, but finite. The addition of the surface tension did not change the shape of the fluid-fluid interface, most likely because the capillary number is still so large since the viscous effects dominate the problem.

5.3.3 Shear-thinning Rheology: Denser Less Viscous Fluid over Less Dense, More Viscous Fluid

We also did simulations in the drawdown geometry using the Carreau fits for the conductive and dielectric materials given in Table IV, but we let the top fluid be denser, but less viscous and the bottom fluid be less dense, but more viscous than the top fluid. This would imply that the Rayleigh-Taylor instability would still be present with the unfavorable density stack against gravity, but there would be some relief from the Kelvin-Helmholtz instability since the viscosities would be more favorably aligned. In these simulations, the viscosity changes with shear-rate similarly to the experimental data. Results using the shear-thinning rheological model are shown in figure 41 and figure 42 as the flow field develops with time for an initial condition of half-filled with each fluid.

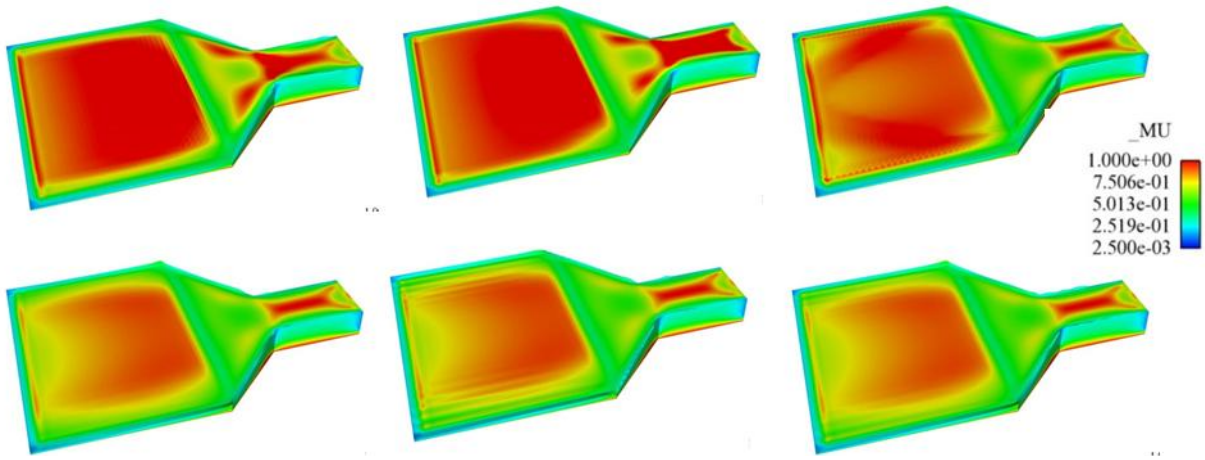

Figure 41: Lower fluid meniscus and evolving dimensionless viscosity with time at 0.5s, 1.0s, 2.0s, 5s, 7s, 10s. A ribbing instability is seen beginning at 5.0s and develops more fully at 7.0s, but starts to damp out at later times. The simulations never reach steady state, but oscillate between two states with the shear surface jumping forward and backwards near the outflow.

From figure 41, we see that this configuration still shows a ribbing instability and this instability begin earlier (at 5.0s instead of 7.0s) and persists longer than the case presented in section 5.3.2 as it is still seen at 10s. Figure 42 shows the viscosity and the meniscus of the upper fluid as a function of time. This is the negative imprint of the lower meniscus shown in figure 41. The viscosity, on average, is higher in the lower fluid.

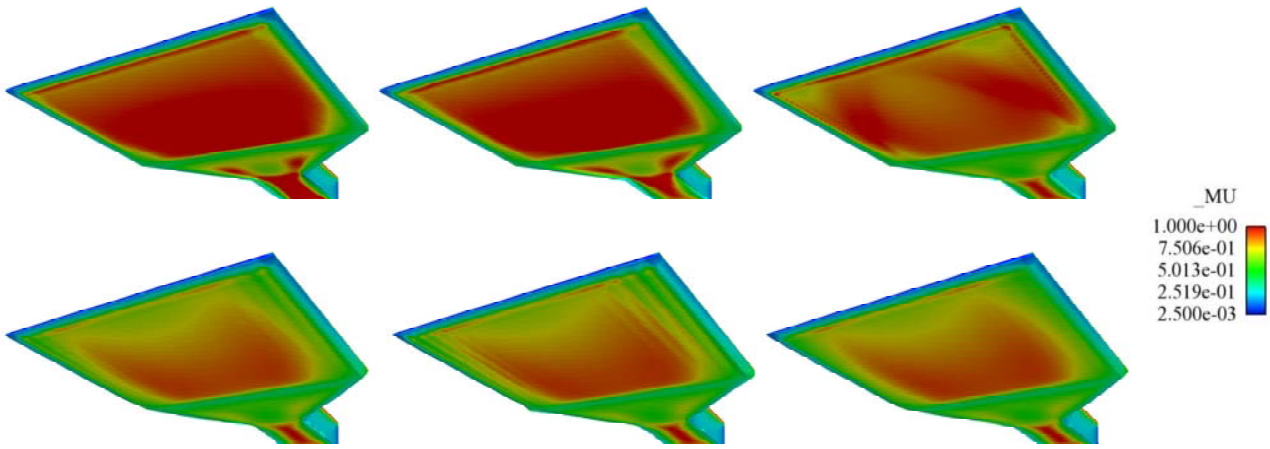

Figure 42: Upper fluid meniscus and evolving viscosity with time at 0.5s, 1.0s, 2.0s, 5s, 7s, 10s. A ribbing instability is seen at 5.0s, increases at 7.0s, but starts to damp out at later times. The simulations never reach steady state, but oscillate between two states with the shear surface jumping forward and backwards near the outflow.

The viscosity in the fluid can be seen more clearly from axial slices of the dimensionless viscosity as it travels down the mold, which is shown in Figure 43, at time of 27.9s.

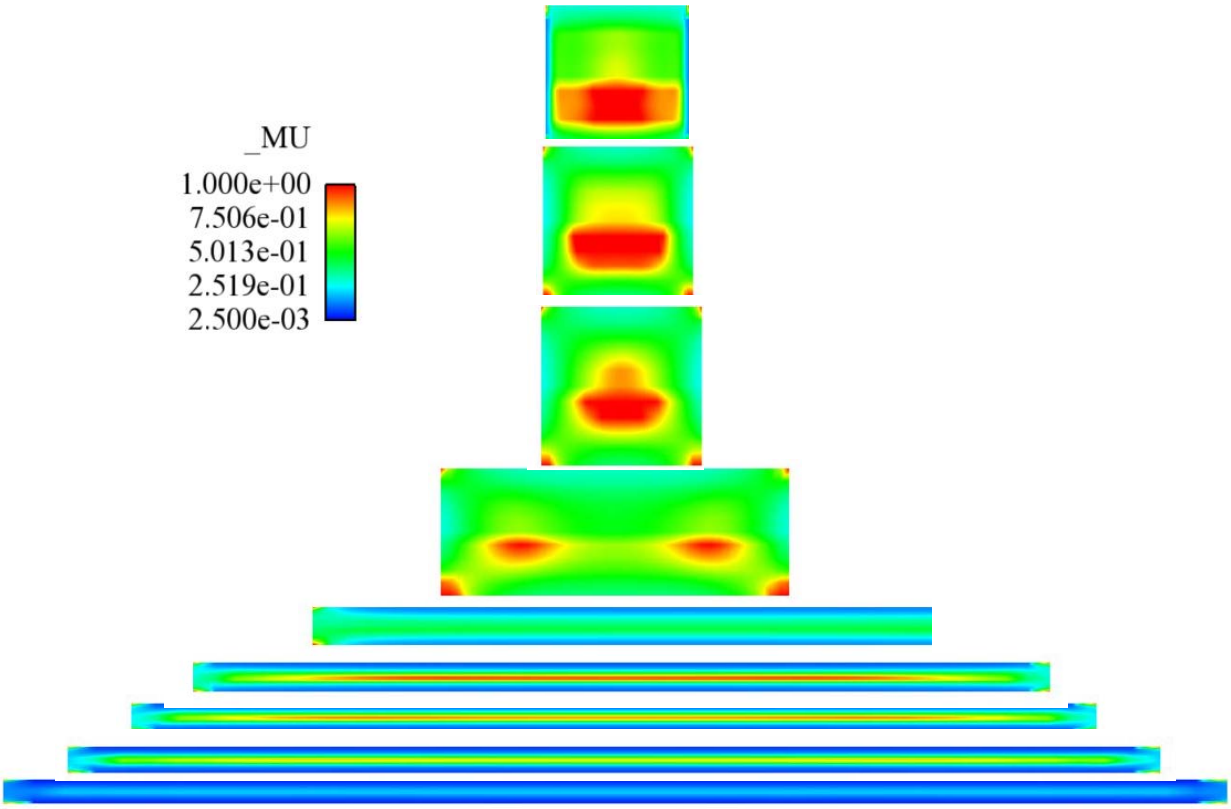

Figure 43: Axial slices of the viscosity as it moves down the mold from the entrance to the drawdown region at 27.9s. (Inflow is at the top of the image and we move axially down the extruder.) The viscosity of the bottom fluid is higher than the top fluid. The density of the top fluid is higher than the bottom fluid.

The more viscous fluid comes in at a higher viscosity indicated by the red color at the bottom of the mold. It shear thins as the mold narrows through the coat hanger section of the die and then shear-thins further as it is extruded through the drawdown region, with high viscosity regions exiting at the center of the die near the interface between the two fluids. High viscosity regions also exist in the bottom corners of the mold, which could also lead to processing difficulties and material accumulating there.

We can also examining the outflow profile as a function of time for this scenario to better understand how stable and flat the layers of extrudate will be (figure 44).

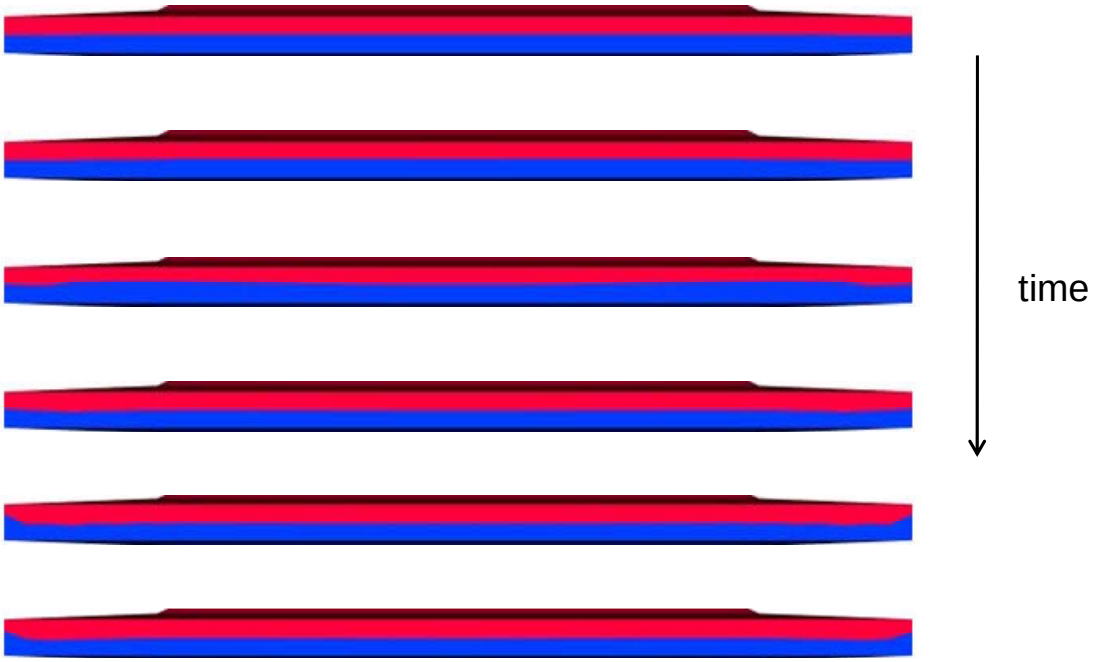

Figure 44: Outflow profile as a function of time for 0.5s, 1.0s, 2.0s, 5s, 7s, 10s

From figure 44, we can see that there is an instability that develops at the edges of the mold that develops over time and looks worst at 10s. The thickness of the bottom fluid is larger than the top fluid. We can also look at the profile at the final time of 29.7s. This is shown in figure 45.

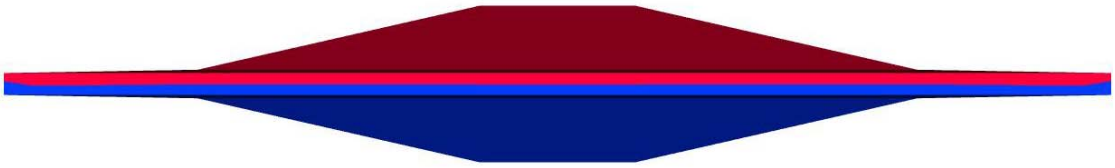

Figure 45: Outflow profile at long times (t=29.4s).

From figure 45, we can see that the edge instability persists over time, but looks less pronounced than in the case where both the density and viscosities are unfavorably positioned with respect to gravity, as we can see from comparing it to figure 40.

5.3.4 Experimental Results from Coextrusion Manufacturing

We also produced a coextruded part using the materials with complex rheology and viscosity and density mismatches discusses above. The part is shown in figure 45 and from this we can see that the model correctly predicted that layers would not remain stable. Thus a poor capacitor was produced.

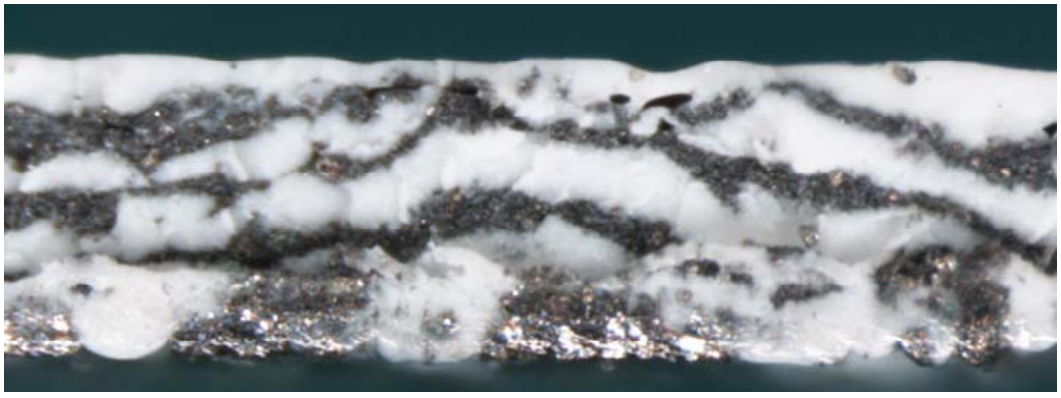

Figure 46: Coextruded eight-layer capacitor showing instabilities present for fluid with both mismatched viscosities and densities

We were able to improve the layer stability by reducing the speed of the more viscous fluid. Results from this experiment are shown in figure 46. By more closely matching the pressure drops between the fluids with mismatched properties we were able to make a capacitor with capacitance in the pico-Farad range.

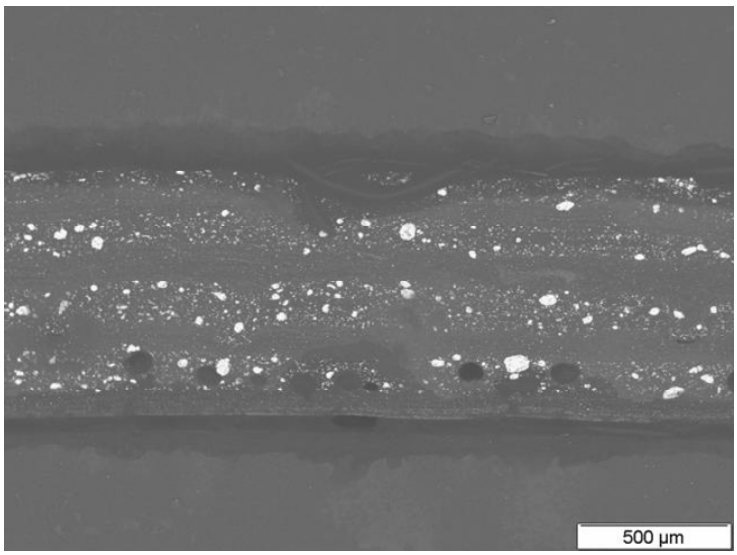

Figure 47: SEM of coextruded capacitor for slower flow rate of more viscous fluid. This process reduces the layer instability seen in figure 46.

6 CONCLUSIONS AND FUTURE WORK

In this report, we have presented a multifaceted numerical study of multilayer coextrusion. We have used linear stability analysis to understand density driven instabilities in a coextruder, while presenting verification of this capability on classic problems with analytical solutions. Scoping simulations were carried out before we had developed conductive and dielectric materials for the capacitor and before their rheology was understood. For these calculations, we assumed the materials were Newtonian and have used two different 3D free surface capabilities to examine coextrusion: an ALE moving mesh algorithm and an Eulerian level set algorithm. We have developed an offset die design that can be used to create coextruded materials where one phase encapsulates the other for applications such as energy storage and sensors. We have also investigated layer-stability through the splitter, where a four layer structure was created from a two layer one, using both ALE and Eulerian methods to understand the effects of different viscosity ratios and pressure drops.

Once the dielectric and conductive material were selected, we did careful rheological measurements in both a parallel plate and capillary rheometer to understand the shear-thinning of the composite materials. This data was fit to a shear-thinning Carreau model and used in 3D level set simulations of the drawdown region where a two-layer structure is sent through a coat-hanger die from an initially square cross-section. This analysis shows that the viscosity and density mismatch between the dielectric and conductive layer will lead to instabilities and differing layer thickness. Experiments confirm this result and have also shown that improved coextruded product can be made by better matching the pressures in the two fluids, as was shown in the scoping calculations.

REFERENCES

3M, 2005, "Multilayer Coextrusion Die and Method," U.S. Patent 6837698

Bird, R. B., Stewart, W.E., Lightfoot, E.N., *Transport Phenomena*, John Wiley and Sons, New York, USA, 1960.

Bird, R. B., Armstrong, R.C., Hassager, O., *Dynamics of Polymeric Liquids*, John Wiley and Sons, New York, USA, 1987.

T.A. Baer; R.A. Cairncross; P.R. Schunk; R.R. Rao; P.A. Sackinger *Int. J. Numer. Meth. Fluids*, 2000, *33*, 405.

Barnes, H. A.; Hutton, J. F.; and Walters, K., 1989, *An Introduction to Rheology*, Elsevier, New York, p. 32.

R.A. Cairncross; P.R. Schunk; T.A. Baer; R.R. Rao; P.A. Sackinger *Int. J. Numer. Meth. Fluids*, 2000, *33*, 375.

Chandrasekhar, S., *Hydrodynamic and Hydromagnetic Stability*. New York, Dover, 1961.

Chung, D. D. L., 2001, *Carbon*, **39**, 279-285.

Computer Support Group, 2009, http://www.csgnetwork.com/dieconstantstable.html

A.T. Crumm; J.W. Halloran *J. Mater. Sci*, 2007, *42*, 1336.

C.R Dohrmann; P.B. Bochev *Int. J. Numer. Meth. Fluids*, 2004, *46*, 183

J. Dooley; L. Rudolf *PFFC online.com*, Jan. 2003, 73.

Dow Global Technology, 2007 "Multilayer Polymer Sheets," U.S. Patent Application 20070184259.

Einstein, A., 1906, *Annalen der Physik*, **19**, 289-306.

Einstein, A., 1911, *Annalen der Physik*, **34**, 591-592.

Farris, R. J., 1968, *Trans. Soc. Rheol*., **12**, 281-301.

Frankel, N. A. and Acrivos, A., 1970, *J. Fluid Mech*. **44**, 65-78.

Gates, I.D., Labreche, D.A., and Hopkins, M. M., "Advanced Capabilities in GOMA 3.0 – Augmenting Conditions, Automatic Continuation and Linear Stability Analysis, SAND2000-2465, January, 2001.

Gerard, M.; Chaubey, A.; Malhorta, B. D., 2002, *Biosens. Bioelectron.*, **17**, 345-359.

Gleissle, W and Hochstein, B, 2003, *J. Rheol*. **47**, 897-910.

Grizzuti, N.; Buonocore, G.; Iorio, G., 2000, J. Rheol. 44, 149-164.

Gupta, R. K., 2000, Polymer and Composite Rheology, 2nd Edition, Marcel Dekker, New York, p. 229.

Huang, C. K. and Cheng, F. S., 2009, *Intern. Polymer Processing*, **XXIV**, 267-271.

T. J. R. Hughes. The Finite Element Method. Dover Publications, New York, USA, 2000.

Kalyon, D. M.; Birinci, E.; Yazici, R.; Karuv, B.; and Walsh, S., 2002, *Polymer Eng. Sci.,* **42**, 1609-1617.

Khomenko, V.; Frackowiak, E.; Beguin, F., 2005, *Electrochim. Acta* **,50**, 2499-2506.

Krieger, I. M. and Dougherty, T, 1959, *Trans. Soc. Rheol.,* **3**, 137-152.

L. Lamnawar; A. Maazouz in *10th ESAFORM Conference on Material Forming*, edited E. Cueto and F. Chinesta, American Institute of Physics, 2007.

Lester, Adam, 2009, Sandia National Laboratories Organization 1732, personal communication.

Macosko, C. W., 1994, Rheology: Principles, Measurements, and Applications, Wiley-VCH, New York, p. 244-247.

Mooney, M., 1951, *J. Colloid Sci*., **6**, 162-170.

Musson, L.C., "Two-Layer Slot Coating," University of Minnesota, Dissertation, 2001.

P. K. Notz, S. R. Subia, M. M. Hopkins, H. K. Moffat, D. R. Noble, ARIA Manual Aria 1.5: User's Manual, SAND2007-2734, Sandia National Laboratories, Albuquerque, NM, April, 2007.

Prud'homme, R. K. and Khan, S. A., 1996, "Experimental Results on Foam Rheology," in *Foams, Theory, Measurements and Applications,* Prud'homme and Khan, Eds., Marcel Dekker, Inc. New York.

L. A. Mondy, R. Mrozek, R. R. Rao, J. Lenhart, L. Bieg, S. Spangler, D. Schneider, M. Stavig, J. Schroeder, M. Winter, P. Cole, "Multilayer Co-Extrusion Technique for Developing High Energy Density Organic Devices," Sandia National Laboratories, SAND2009-7718, October, 2009.

Rayleigh, F.R.S., "On the Instability of Jets," *Proceedings of the London Mathematical Society*, 10: 4–13, November, 1878.

Rincon, A. J.; Hrymak, A. N.; Vlachopoulos, J., 1998, *Int. J. Numer. Meth. Fluids*, **28**, 1159.

Renardy, M., 1997, *J. Non-Newtonian Fluid Mech.* **68**, 125-132.

P.R. Schunk; P.A. Sackinger; R.R. Rao; K.S. Chen; T.A. Baer; D.A. Labreche; A.C. Sun; M.M. Hopkins; S.R. Subia; H.K. Moffat; R.B. Secor; R.A. Roach; E.D. Wilkes; D.R. Noble; P.L. Hopkins; P.K. Notz; "GOMA 5.0 – A Full-Newton Finite Element Program for Free and Moving Boundary Problems with Coupled Fluid/Solid Momentum, Energy, Mass, and Chemical Species Transport: User's Guide," Sandia National Laboratories, SAND2006-5375/1, October, 2006.

Tao, W. H.; Chen, C.; Ho, C. E.; Chen, W. T.; Kao, C. R., 2001, *Chem. Mater.*, **13**, 1051-1056.

Taylor, G. I. 1934, *Proc. Roy. Soc. Ser. A.* **146**, 0501-0523.

Thomas, D. G., 1965, *J. Colloid Science*, **20**, 267-277.

Wang, Shi-Qing; Drda, Patrick, 1997, *Macromol. Chem. Phys*., **198**, 673-701.

Wessling, B., 1998, *Synth. Met.*, **93**, 143-154.

Yang, Ping, 2009, personal communication.

Zhao, R; Macosko, C. W., 2002, *J. Rheol.* **46**, 145-167.

7 DISTRIBUTION

1	MS0346	Lisa Mondy	1514	
1	MS0836	P. Randall Schunk	1516	
1	MS0836	Rekha Rao	1514	
1	MS0886	Jim Aubert	1822	electronic copy
1	MS0888	Regan Stinnett	1821	electronic copy
1	MS0958	Mike Kelly	2453	electronic copy
1	MS0899	Technical Library	9536	electronic copy
1	MS0359	D. Chavez, LDRD Office	1911	


Sandia National Laboratories